

Design and Concept of Mars Microprobe Mission Architecture

Liam Piper*

Independent Researcher, Norwich, CT, 06360.

The Mars Atmospheric and Ground Probe Instrumentation Experiment (MAGPIE) is a distributed lander mission concept deploying six autonomous microprobes from a dedicated relay orbiter to obtain time-synchronous meteorological, electrical, and visual measurements across a pole-to-pole latitude range on Mars. The mission architecture calculates a 276 day heliocentric transfer prior to Mars Orbit Insertion, followed by sequential probe releases timed to low-altitude orbital passes. After landing, the average probe is designed for a 28 sol operational window, while polar deployments are expected to operate for at least 32 hours under low-insolation conditions. Each 23 kg probe utilizes a 1 m diameter, 70 degree sphere-cone aeroshell, drogue and main parachutes, and an aluminum based honeycomb crush-core landing system designed to absorb more than 90% of terminal kinetic energy from landing. High-fidelity entry-descent-landing (EDL) simulations predict peak decelerations of 12 g and computed terminal velocities of 14 m/s, remaining within structural and thermal limits across representative dispersions. The orbiter is designed with dual-frequency Ultra High Frequency (UHF) and Long Range (LoRa) relay links and an X-band Deep Space Network (DSN) downlink, supported by a redundant Attitude Determination and Control System (ADCS) architecture with primary reaction wheels, secondary wheels, tertiary wheels, dual star trackers, coarse sun sensors, and a computer-vision star-tracking mode. Mission trajectory and propulsion modeling indicates that a Falcon 9 launch vehicle can deliver the 7.5 t integrated stack onto a C₃ of 9.879 km²/s² with a 10% performance margin. A 700-hour landed thermal, power and, communication simulation suggests sustained, net power positive operation at mid-latitudes under moderate dust loading ($\tau = 0.4$), with all critical nodes maintained above survival thresholds.

I. Nomenclature

Atmospheric Entry and Aerodynamics

A	= Reference area of aeroshell or parachute
A_{ref}	= Aeroshell aerodynamic reference area
C_D	= Drag coefficient
C_L	= Lift coefficient
L/D	= Lift-to-drag ratio
β	= Ballistic coefficient $m/(C_D A_{\text{ref}})$
M	= Mach number
q	= Dynamic pressure (Pa)
ρ	= Atmospheric density (kg/m ³)
E_I	= Entry interface altitude
s	= Crush-core stroke distance
σ_p	= Crush plateau stress of honeycomb core

Trajectory and Propulsion

C_3	= Characteristic energy of Earth escape
V_∞	= Hyperbolic excess velocity at arrival/departure
Δv	= Change in velocity
I_{sp}	= Specific impulse

*Independent Mission Design Lead, MAGPIE Project. B.S. in Aerospace Engineering from Worcester Polytechnic Institute. AIAA Member Number: 1601426 .

TOF	=	Earth–Mars time of flight
g_0	=	Standard gravity ($9.806\,65\text{ m/s}^2$)
MOI	=	Mars Orbit Insertion
TMI	=	Trans-Mars Injection

Thermal and Power

P_{gen}	=	Generated electrical power
P_{load}	=	Electrical load excluding heaters
SOC	=	Battery state of charge
$R_{\text{skin}\rightarrow\text{int}}$	=	Thermal resistance (skin \rightarrow interior)
$R_{\text{int}\leftrightarrow\text{batt}}$	=	Thermal resistance (interior \leftrightarrow battery)
τ	=	Optical depth (dust opacity)

Communications

P_t, P_r	=	Transmit and received power
T_s	=	System noise temperature
HGA	=	High-gain antenna
UHF	=	Ultra High Frequency (403–437 MHz)
LoRa	=	Long-range, low-power modulation scheme

Guidance, Navigation, and Control

\mathbf{q}	=	Attitude quaternion (inertial to body)
ω	=	Body angular rates
\mathbf{h}_w	=	Total stored reaction-wheel angular momentum
$\boldsymbol{\tau}_c$	=	Commanded control torque
θ_0	=	Slew angle or commanded attitude displacement
EKF	=	Extended Kalman Filter
CSS	=	Coarse Sun Sensor
RW	=	Reaction wheel
CV	=	Computer-vision star-tracking mode

Orbiter/Probe Systems

LMO	=	Low Mars Orbit
PMD	=	Propellant Management Device
$COPV$	=	Composite Overwrapped Pressure Vessel
P_{tank}	=	Propellant tank pressure
V_{tank}	=	Propellant tank internal volume
He	=	Helium pressurant gas
N_2	=	Nitrogen cold-gas propellant (probe)

II. Introduction

THE Mars Atmospheric & Ground Probe Instrumentation Experiment (MAGPIE) mission concept represents a low-cost, distributed approach to Martian surface science. Six identical microprobes are deployed from a dedicated relay orbiter to diverse latitudes, providing simultaneous meteorological, electrical, and visual measurements. The mission's overarching goal is to characterize the temporal and spatial structure of the Martian boundary layer, yielding a climatological and physical dataset that informs both atmospheric science and future mission design.

This paper presents an integrated analysis of the MAGPIE mission architecture, encompassing scientific motivation, trajectory design, entry–descent–landing (EDL) modeling, probe design, cost estimation, and surface environmental survivability supported by high-fidelity thermal–power simulations.

A key feature of the architecture is the flexibility of probe deployment. The destination of each probe, as well as the total number of deployed units, can be adapted *in situ* based on available launch mass and evolving science priorities. The modular probe–aeroshell stack can also be flown as a secondary payload on commercial rideshare missions or vehicle demonstration missions, enabling low-cost technology demonstrations in a relatively low-risk environment prior to committing to a full network deployment.

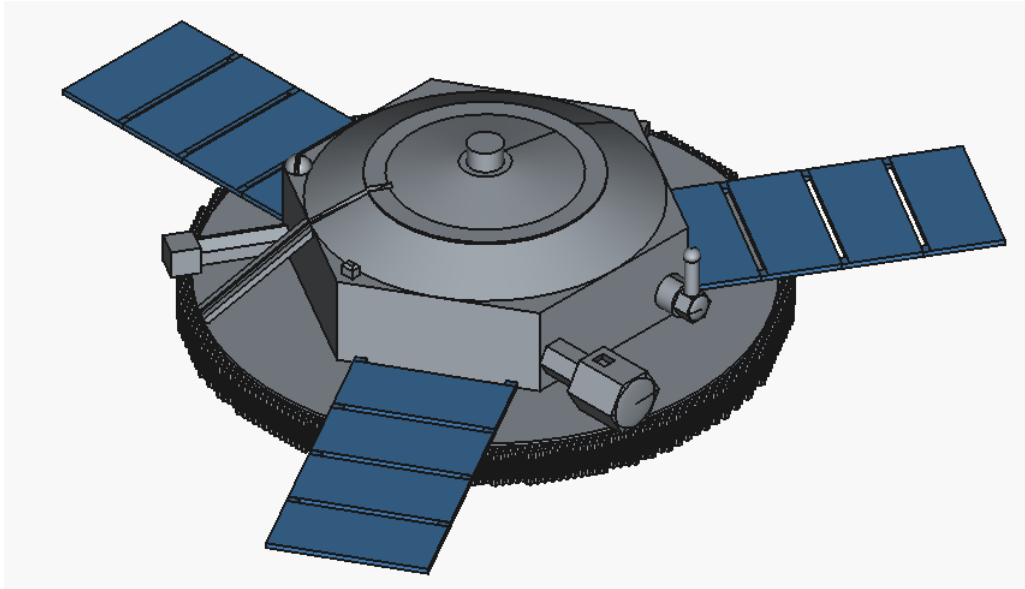


Fig. 1 A deployed MAGPIE probe.

A. Mission Timeline

The MAGPIE mission proceeds through a structured cruise–EDL–surface sequence designed to maximize science return from a globally distributed probe network. Following launch, the spacecraft departs Earth on a heliocentric transfer with a total time-of-flight (TOF) of approximately 276 days, culminating in Mars Orbit Insertion (MOI) and transition into the relay science orbit.

Probe deployment occurs over successive low-altitude orbital passes to ensure accurate entry targeting and consistent relay visibility. Each probe executes atmospheric entry, drogue and main parachute deployment, and a low-velocity landing supported by a crush-core impact system.

Once on the surface, each mid-latitude and equatorial probe is designed for a nominal operational lifetime of 28 sols, enabling continuous meteorological, electrical, acoustic, and imaging measurements. Probes delivered to the polar regions, where insulation and thermal margins are severely constrained, are guaranteed a minimum operational duration of 32 hours, sufficient to capture at least one complete diurnal cycle before battery depletion.

From a system-level perspective, the mission spans interplanetary cruise, orbit insertion, sequential probe releases, and a multi-week (28 Sol) surface campaign. Throughout this period, the relay orbiter maintains daily communication passes for data return and time-synchronized observations across the MAGPIE probe network.

III. Science Objectives and Measurement Approach

The Mars Atmospheric & Ground Probe Instrumentation Experiment (MAGPIE) is designed to perform distributed, time-synchronous measurements of the Martian lower atmosphere spanning equatorial to polar latitudes. The mission deploys six identical microprobes, each equipped for both descent and landed operations, providing comprehensive vertical and horizontal context for meteorological, electrical, and aeolian processes. Through coordinated timing and orbital relay support, MAGPIE enables continuous global sampling of boundary-layer phenomena and atmospheric electrification dynamics.

The core scientific objectives of MAGPIE are as follows:

- 1) **Characterize boundary-layer meteorology.** Measure pressure, temperature, humidity, and wind velocity across local times and latitudes to quantify the diurnal and seasonal atmospheric structure.
- 2) **Investigate atmospheric electrification.** Observe DC–AC electric field variability associated with dust lifting, saltation, and convective storm development.
- 3) **Correlate meteorological, electrical, and visual phenomena.** Integrate meteorological data with imaging and acoustic diagnostics to examine coupling between dust, frost, turbulence, and microseismic activity.

To accomplish these goals, the probes will land at multiple sites across different longitudes and latitudes. Landing sites are chosen to maximize scientific return while ensuring safe descent and consistent communication windows with the orbiter.

MAGPIE-1 is planned for the northern slope of Olympus Mons to observe upper-level winds, mountain-driven cloud formation, and how the landscape shapes small-scale weather.

MAGPIE-2 is assigned to Hellas Planitia, the deepest known impact basin on Mars. Its low elevation presents an opportunity to study high-pressure boundary-layer behavior and enhanced dust loading in a basin environment. It is a high-priority study location due to favorable conditions for future human exploration.

MAGPIE-3 will land in Planum Boreum, the north polar region, during the late summer season to observe CO₂ frost sublimation and polar cap retreat dynamics.

MAGPIE-4 is deployed to Planum Australis, the south polar counterpart, providing a mirror dataset to MAGPIE-3 for hemispheric comparison of volatile cycles and cold-season meteorology.

MAGPIE-5 and 6 are reserved for sites selected along the equator-crossing orbital track, focusing on regions of future human landing interest or serving as flexible backups. These locations ensure operational diversity and provide redundancy in the event of entry anomalies at other sites. This configuration enables the MAGPIE network to span from +90° to –90° latitude, capturing the vertical and horizontal structure of Martian near-surface processes with temporal coherence. Each probe release is timed to its orbital pass to ensure accurate targeting and clear descent trajectories. The final science orbit geometry ensures at least one ten-minute line-of-sight communication window per site per orbit, allowing reliable daily data return throughout the mission.

Table 1 MAGPIE Probe Landing Sites Overview

Probe	Landing Site	Coordinates
MAGPIE-1	Olympus Mons	18.65°N, 226.2°E
MAGPIE-2	Hellas Planitia	42.4°S, 70.5°E
MAGPIE-3	Planum Boreum	87.98°N, 15.0°E
MAGPIE-4	Planum Australis	83.9°S, 160.0°E
MAGPIE-5 and 6	Mission Backups	N/A

These distributed measurements provide pole-to-pole correlation of transient meteorological and electrical events, such as regional dust storms and boundary-layer oscillations, offering an unprecedented dataset for comparative climatology and for improving EDL environment modeling.

IV. Instrument Suite and Methods

Each MAGPIE probe incorporates a compact, integrated instrument suite tailored to the constraints of low-mass surface delivery and extended autonomous operation. Table 2 summarizes the instrument classes and their corresponding measurement domains. In addition to in-situ sensing, MAGPIE leverages radio occultation of the orbiter–probe and orbiter–Earth links to retrieve vertical profiles of refractivity, and thus temperature and density, along the radio signal path.

Table 2 MAGPIE Instrument Suite Overview

Subsystem	Description and Capabilities
Meteorology	Pressure (± 0.5 Pa), temperature (± 0.1 K), humidity ($\pm 2\%$ RH), and CO ₂ concentration (ppm-level). Includes a solid-state thermal anemometer (± 40 m/s, 10–50 Hz sampling).
Electrification	Broadband electric-field antenna with low-noise preamplifier (DC–100 kHz bandwidth), providing quasi-static and AC field measurements.
Acoustics	Wideband microphone (20 Hz–12 kHz) for detection of wind turbulence, dust impacts, mechanical events, and microseismic activity.
Navigation and Descent Profiling	ADIS16470 nine-axis IMU providing: <ul style="list-style-type: none"> Gyroscopes: $\pm 2000^\circ/\text{s}$ range; 8 deg/hr in-run bias stability; 0.008 deg/s/$\sqrt{\text{Hz}}$ noise density. Accelerometers: ± 40 g range; 13 μg in-run bias stability. Bandwidth: 600 Hz (3 dB) for accelerometers. Sampling: Internal rate of 2000 SPS (IMU data decimated to 200 Hz for GNC). Environmental: -25°C to $+85^\circ\text{C}$ operating range; 2000 g shock survivability. Interface/Power: SPI digital output; 3.0–3.6 V supply; 42–50 mA typical current draw. Supplemented by a nadir radar altimeter (20 Hz) and a tri-axis magnetometer for coarse orientation and descent characterization.
Imaging	Side color camera (horizon-facing; still or burst modes), nadir-facing descent camera, and thermal IR imager for temperature-contrast mapping of dust, frost, and cloud structures.

A. Measurement Concept

Each probe records high-frequency (10–200 Hz) meteorological and electrical data during descent and continues periodic sampling after landing. Synchronized operation of the six units enables spatial correlation of near-surface atmospheric parameters across hemispheres. Acoustic and imaging payloads provide context for dust lifting, vortex formation, and surface–atmosphere coupling. The diversity of sampling rates reflects the distinct operational modes and physical response times of the instruments.

Additionally, the orbiter monitors carrier-phase and amplitude variations during radio occultations of the probe–orbiter and orbiter–Earth links. Inversion of these profiles yields vertical structure in refractivity, which can be mapped to temperature, density, and pressure under standard assumptions about atmospheric composition. The combination of point in-situ measurements, descent profiles, and occultation-derived vertical structure provides a multi-scale view of the Martian lower atmosphere, contributing to a broader understanding of the system state at the time of observation.

B. Calibration and Data Products

Meteorological sensors are calibrated against terrestrial analog instrumentation prior to launch and validated using Mars-environment chamber tests. Electric-field antennas are cross-validated in plasma chambers to ensure linear response over their quasi-static and AC ranges. Primary data products include:

- Time-stamped meteorological vectors
- Electric-field power spectra and transient waveforms
- Reconstructed descent trajectories and attitude histories

- Image-derived optical flow metrics and dust opacity estimates
- Occultation-derived vertical profiles of refractivity, temperature, and density.

V. Mission Design and Trajectory Analysis

The MAGPIE trajectory is designed to (1) fit within the performance envelope of a commercially available launch vehicle, (2) provide benign Mars arrival conditions for orbit insertion, and (3) yield relay geometries compatible with simultaneous probe EDL. This section summarizes the selection of the Earth–Mars transfer, the resulting injection requirements, and the launch vehicle trade that led to the Falcon 9–class baseline.

A. Transfer Window and Injection

One of the most important design decisions in a Mars mission is the selection of the transfer window. For a chemically propelled spacecraft, Earth–Mars opportunities recur roughly every 26 months, but the corresponding characteristic energy C_3 and time of flight (TOF) can vary substantially from opportunity to opportunity. Early design work on MAGPIE assumed a conjunction-class, Type-I trajectory in which the spacecraft completes less than 180° of heliocentric motion between departure and arrival [1].

A porkchop analysis over the 2026–2030 opportunities was performed using heliocentric Lambert solutions and patched-conic departure/arrival modeling. Each candidate trajectory was evaluated against:

- launch energy (C_3) and required departure Δv
- time of flight and associated cruise-phase operations burden
- Mars arrival V_∞ and orbit insertion Δv
- seasonal and local-time conditions at the anticipated probe EDL dates.

For a given departure date, the characteristic energy is defined as

$$C_3 = V_{\infty,\text{dep}}^2, \quad (1)$$

where $V_{\infty,\text{dep}}$ is the hyperbolic excess velocity at Earth departure. The required injection Δv from low Earth orbit (LEO) is approximated as

$$\Delta v_{\text{TMI}} \approx \sqrt{V_{\text{esc}}^2 + C_3} - V_{\text{LEO}}, \quad (2)$$

with V_{esc} the local escape speed at the parking-orbit radius and V_{LEO} the circular velocity [1].

The selected solution departs 20 November 2028 and arrives 23 August 2029 with TOF = 276 days, $C_3 = 9.879 \text{ km}^2 \text{ s}^{-2}$, and departure $\Delta v_{\text{TMI}} = 3.634 \text{ km s}^{-1}$. This point lies near the interior of the low- C_3 valley in the porkchop plot, providing a good compromise between launch energy and cruise duration while keeping the Mars arrival V_∞ low enough to minimize orbit-insertion Δv .

Shorter-TOF trajectories in the same window were rejected because they required higher C_3 and increased Mars arrival speed, driving both upper-stage performance and MONARC propellant mass. Conversely, very low- C_3 options existed at the cost of substantially longer cruise durations (10–12 months), which would increase operational complexity, thermal control burden, and cumulative radiation exposure for the orbiter avionics.

The trans-Mars injection (TMI) is performed by the Falcon 9 upper stage from an initial LEO parking orbit. Using a mixture-ratio-aware model ($I_{sp} = 348 \text{ s}$, O/F = 2.56) and assuming a typical LEO insertion by the first stage, approximately 27 tons of propellant remain available in the second stage at the start of TMI. This provides $\sim 6.4 \text{ km/s}$ of ideal Δv capability, leaving roughly 25% margin after the 3.634 km/s TMI burn when guidance losses and residuals are included.

The resulting heliocentric trajectory is shown in Fig. 2. The orbit is broadly Hohmann-like, with a modest inclination offset driven by the relative geometry of Earth and Mars at the chosen dates. The arrival geometry is compatible with a direct, propulsive capture into a highly elliptical Mars orbit without aerocapture [2].

A refined porkchop search around the 2028–2029 opportunity identified a narrow corridor of low- C_3 solutions spanning mid–November to early December 2028. The twelve best departures by required LEO $\rightarrow C_3 \Delta v$ all clustered between 10 November and 2 December, with time of flight fixed at 275–276 days and departure Δv ranging from 3.634 to 3.729 km s $^{-1}$. The selected trajectory, departing 20th November 2028, lies near the center of this low- Δv trough (Table 3), providing robustness against a few days of launch slip while keeping both TMI and Mars-arrival conditions near optimal [1].

Table 3 Top departure candidates from porkchop analysis (ranked by departure Δv).

Rank	Departure Date	TOF (days)	Δv_{TMI} (km/s)
1	2028-11-20	276	3.634
2	2028-11-22	276	3.636
3	2028-11-18	276	3.638
4	2028-11-24	276	3.643
5	2028-11-16	276	3.646

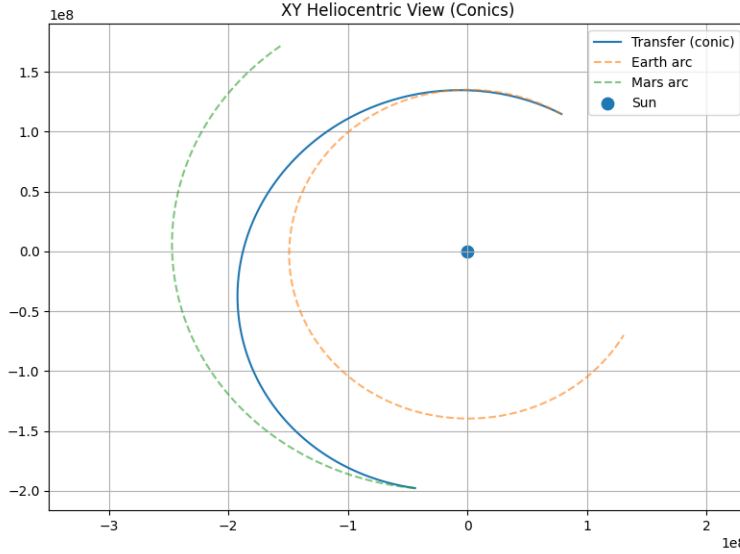


Fig. 2 XY heliocentric view of the Earth–Mars transfer trajectory for the selected 2028 window.

B. Launch Vehicle Trade Study

The MAGPIE mission architecture requires delivery of the combined orbiter and six-probe stack to a low Mars orbit (LMO) following a direct Earth-to-Mars transfer. Candidate launch vehicles considered included the Falcon 9 and Falcon Heavy of SpaceX, as well as the Vulcan Centaur of United Launch Alliance and other emerging systems such as New Glenn (Blue Origin). The trade was evaluated using technical and programmatic criteria: performance to high C_3 , cost per kilogram delivered, reliability and heritage, fairing volume, schedule, and export/regulatory risk.

Performance Analysis. The payload stack, including the orbiter and attached de-orbit probes, has a mass of approximately 7,485 kg at LEO. This corresponds to 32.8 % of the nominal Falcon 9 LEO capacity (22,800 kg) [3]. A simplified ascent and trans-Mars injection (TMI) analysis was performed using mixture-aware modeling of the Falcon 9 second-stage Merlin 1D Vacuum (MVac) engine, which has $I_{\text{sp}} = 348$ s and mixture ratio $O/F = 2.56$. The stage parameters are summarized in Table 4.

The low-energy trans-Mars trajectory for the reference 2029 window requires a characteristic energy of $C_3 \approx 10 \text{ km}^2/\text{s}^2$, equivalent to a hyperbolic excess velocity $v_\infty = \sqrt{C_3} = 3.16 \text{ km/s}$. The MVac stage provides this required Δv directly from a circular LEO parking orbit without the need for an auxiliary kick stage:

$$\Delta v_{\text{LEO} \rightarrow C_3} = 3.634 \text{ km/s}, \quad (3)$$

$$m_{\text{payload}} = 7.485 \text{ t}, \quad (4)$$

$$m_{\text{prop, used}} = 55.4 \text{ t}. \quad (5)$$

The corresponding mass fraction is [4]

$$\lambda = \frac{m_{\text{payload}} + m_{\text{dry}}}{m_{\text{dry}} + m_{\text{prop}} + m_{\text{payload}}} = 0.12,$$

Table 4 Falcon 9 Second-Stage Ascent and Injection Parameters

Parameter	Value	Unit
Total propellant load (LOX+RP-1)	110,000	kg
Dry mass (stage)	6,250	kg
LOX mass fraction	71.9	%
RP-1 mass fraction	28.1	%
Initial orbital payload	7,485	kg
Launch adapter	1,382	kg
Stage Δv capability	6.20	km/s
Δv required for MAGPIE transfer	3.63	km/s
Propellant expended for TMI	55,413	kg
Remaining propellant after TMI	26,419	kg (24.0%)

consistent with the expected performance envelope for a Falcon 9 to $C_3 = 10 \text{ km}^2/\text{s}^2$.

Reduction in Offloaded Payload Mass. Recasting the mission to use the launch-vehicle orbital stage (Orbital Module) for the TMI burn substantially reduces the injected payload mass. Early MAGPIE design cycles assumed a solid-propellant kick stage (e.g., STAR 48/65 class) riding above a conventional LEO insertion, which drove the required injected mass into the 10–11 tonne class. In the present architecture, the Falcon 9 second stage both circularizes to LEO and performs the full TMI burn, eliminating the separate kick stage and its structural/interstage penalty. For the same 7.485 tonne orbiter+probe stack, the required injection mass is thereby reduced by roughly 25–30 %, which allows the entire stack to fit comfortably within a Falcon 9–class vehicle while still preserving science mass and structural margins [4].

Trade Summary. Each candidate vehicle was evaluated against:

- **Performance to C_3 :** ability to deliver a payload with $C_3 \geq 10 \text{ km}^2/\text{s}^2$ including 10–20 % margin.
- **Cost per delivered kilogram:** for example, Falcon 9 offers a price point of approximately \$2,600–3,000 USD/kg to LEO based on public list price and capacity [3].
- **Reliability and heritage:** flight record and interplanetary mission experience.
- **Fairing volume and payload accommodation:** including payload envelope, adapter interface, and separation environment.
- **Schedule flexibility and programmatic risk:** cadence, manifest backlog, reflight options, export control.

While Falcon Heavy offers significantly greater trans-Mars performance (for example, $C_3 > 20 \text{ km}^2/\text{s}^2$ and of order 16 tonnes to Mars escape), its cost and logistical complexity were judged unnecessary for the current ~ 7.5 tonne payload class. ULA’s Vulcan Centaur provides comparable performance to Falcon 9 but with less operational heritage and higher expected cost per mission.

Thus Falcon 9 was baselined for MAGPIE because it combines:

- proven reliability and high launch rate
- sufficient performance with 20–30 % margin to the required C_3
- compatibility with existing ground support infrastructure and potential rideshare options
- cost efficiency and established contracting mechanisms.

Anchoring the mission to a Falcon 9–class capability also ensures portability to similar medium-lift vehicles in the future, preserving programmatic robustness.

Alternative Medium- and Heavy-Lift Launchers. Because the MAGPIE injected mass requirement has been reduced, a number of other medium- and heavy-lift vehicles become technically viable. Below is a comparative summary of representative vehicles, with cost, capacity, and regulatory/heritage context included.

New Glenn. Blue Origin’s New Glenn is particularly attractive from a cost and performance standpoint. Publicly available material indicates a nominal payload capacity of order 45 t to LEO with a large reusable first stage and a

Table 5 Representative medium/heavy-lift launch vehicle options (public list prices 2024–2025) for MAGPIE-class payloads

Vehicle	LEO capacity [t]	Indicative price [M\$]	Approx. cost per kg [\$/kg]
Falcon 9 (Block 5)	22.8	62–70	2,700–3,000
New Glenn (2-stage)	45	68–110	≈ 1,500 (if fully utilized)
Ariane 6 A64	~ 25	98–115	≥ 4,000
Vulcan Centaur	27.2	110–150	~ 4,000–5,500
Long March 5	25–32	100–160	~ 3,100–4,500
Proton–M/Briz–M	21–23.7	~ 65	~ 2,700

7 m-class fairing [5]. Combined with estimated per-launch prices in the \$68–110 M range [6], this yields a potential cost per kilogram as low as ~ 1,500 \$/kg when the vehicle is heavily utilized. For a MAGPIE-class payload of only 7.5 t, however, most of that capacity is unused, so the absolute mission cost advantage relative to Falcon 9 is modest once fixed vehicle and operations costs are accounted for. At the time of this study, New Glenn also has comparatively limited flight heritage, which increases perceived schedule and reliability risk for a first-of-a-kind Mars mission.

Nevertheless, New Glenn represents a highly capable future option for follow-on MAGPIE-class missions or scaled architectures. Its high lift capacity and large fairing could support:

- expanded probe constellations or additional orbiters,
- heavier science payloads and more aggressive propellant margins,
- multi-manifest missions where MAGPIE rides with other large payloads, improving effective cost per kilogram.

As New Glenn accumulates flight history and its operational model matures, it could become the most economical Western option for large, distributed Mars probe networks building on the MAGPIE architecture.

Ariane 6. Europe’s Ariane 6 in the A64 configuration offers ~ 25 t to LEO but at relatively high cost (of order \$100 M per launch), corresponding to a cost per kilogram above \$4,000 [7, 8]. While Ariane 6 provides strong export/regulatory independence for European-led missions and has ample fairing volume for MAGPIE, its higher per-mission cost and lower expected cadence make it less attractive economically for a cost-limited, U.S.-led Mars science mission.

Long March 5. China’s Long March 5 provides ~ 25–32 t to LEO and has demonstrated high-energy mission capability (lunar sample return and Mars missions) [9, 10]. Estimated launch costs of \$100–160 M imply a cost per kilogram in the \$3,100–4,500 range. Although technically well-suited to MAGPIE in terms of performance and fairing size, export-control and partnership constraints render Long March 5 effectively unavailable for this mission concept.

Vulcan Centaur. ULA’s Vulcan Centaur offers ~ 27.2 t to LEO with strong performance to high C_3 [11]. Projected launch prices in the \$110–150 M range [12] yield a cost per kilogram significantly higher than Falcon 9. Combined with lower expected launch cadence in the late 2020s, Vulcan is considered technically capable but less cost-effective for MAGPIE.

Proton–M/Briz–M. The Russian Proton–M with Briz–M upper stage can deliver approximately 21–23.7 t to LEO at an estimated cost of ~ \$65 M, implying a cost per kilogram comparable to Falcon 9 [13, 14]. However, its aging hypergolic architecture, announced phase-out, and geopolitical constraints make it unsuitable as a baseline launcher for a Western Mars science mission in the late 2020s.

Cost Sensitivity Analysis. A simple sensitivity model for MAGPIE assumes that launching on a given vehicle incurs a largely fixed per-mission cost and that performance margin (unused lift capacity) does not linearly reduce cost. For illustration, let

$$\text{Launch Cost} = C_{\text{base}} + \alpha \cdot \left(\frac{m_{\text{payload}}}{m_{\text{capacity}}} \right),$$

where C_{base} is the fixed cost, α a scaling factor, $m_{\text{payload}} = 7.485$ t, and m_{capacity} is the LEO capacity of the vehicle.

Using cost-per-kilogram estimates from Table 5, several observations emerge:

- A vehicle with cost per kg of 3,000 \$/kg (for example, Falcon 9 at full utilization) would imply a notional cost of ~ \$22.5 M for a fully loaded 7.5 t, but the actual list price is ~ \$62–70 M; fixed cost dominates the price.
- For New Glenn (capacity ~ 45 t, cost ~ \$68–110 M, nominally ~ 1,500 \$/kg when fully utilized), using only 7.5 t reduces the payload fraction to ~ 17%. If cost scales weakly with this fraction, the marginal cost saving relative to Falcon 9 is limited; fixed infrastructure and vehicle cost still dominate.
- Therefore, for under-utilized missions in the 5–10 t range, cost sensitivity to vehicle capacity is low; the decision is dominated by fixed cost, reliability, and heritage rather than marginal cost per kilogram.
- If the payload mass were increased (for example, additional probes, instruments, or propellant margins) to 9–15 t, the effective cost per kilogram for high-capacity vehicles like New Glenn improves, potentially making them more attractive for future, scaled-up MAGPIE variants.

A conceptual plot of cost per kilogram versus payload utilization across vehicles would show that for small to moderate payloads (5–10 t) the cost-efficiency benefit of very large vehicles is diluted. The break-even point where a higher-capacity launcher becomes cost-advantageous typically occurs when utilization rises above roughly 40–50 %.

Rationale for Baseline Launcher Selection. Given the specific MAGPIE payload (~ 7.5 t to $C_3 \approx 10 \text{ km}^2/\text{s}^2$), the launch trade is driven less by raw performance and more by mission-level cost, risk, schedule, and heritage. Vehicles like New Glenn and Long March 5 offer lower nominal cost per kilogram in theory but provide limited absolute cost savings for a 7.5 t payload that under-utilizes their capacity, while introducing additional schedule or regulatory risk. Ariane 6 and Vulcan Centaur are significantly higher in both cost per kilogram and per-mission cost, and may carry higher programmatic risk in cadence. In contrast, Falcon 9 offers:

- sufficient performance with comfortable margin (22.8 t capacity versus 7.5 t required),
- extensive flight heritage and multiple interplanetary missions,
- the lowest absolute per-mission cost among Western vehicles for this payload class, and
- a high launch cadence and mature operations model.



Fig. 3 Orbiter Module + Probes + Vehicle Adapter. The Falcon 9 fairing is plenty spacious for the MAGPIE Mission.

Therefore, Falcon 9 remains the most cost-effective and programmatically robust choice for the initial MAGPIE mission. At the same time, the reduced injected mass resulting from the orbital-stage TMI architecture preserves portability to vehicles such as New Glenn, Ariane 6, Vulcan, or Long March 5 should future partnerships, mission expansions, or follow-on MAGPIE constellations justify a different launcher with higher capacity and lower effective cost per kilogram.

C. Trans-Mars Injection and Mars Orbit Insertion

After Earth departure, the Falcon 9 upper stage performs the entire trans-Mars injection (TMI) maneuver, placing the MAGPIE stack onto the selected heliocentric transfer. No dedicated kick stage (e.g., STAR 48B) is required in the baseline configuration, although such a stage remains a growth option for higher- C_3 windows or heavier orbiter variants.

Using the mixture-aware model described above ($I_{sp} = 348$ s, $O/F = 2.56$), the ascent ledger indicates that approximately 55,413 kg of LOX/RP-1 are consumed in the LEO → C_3 burn to deliver $\Delta v_{TMI} = 3.634 \text{ km s}^{-1}$ for a payload mass of 7,485 kg. This leaves 26,419 kg of second-stage propellant (24% of the tank load) as residual margin for guidance dispersions, attitude control, and conservative modeling assumptions. The stage therefore provides the required $C_3 = 9.879 \text{ km}^2 \text{ s}^{-2}$ with substantial performance headroom, confirming the viability of a single-launch Falcon 9 architecture.

Upon Mars arrival, capture and orbit circularization are performed entirely by the orbiter's MONARC-1 propulsion stage. The arrival scenario assumed in this study targets a periapsis altitude of approximately 40 km, for which a minimal aerocapture strategy would require about $0.98\text{--}1.14 \text{ km s}^{-1}$ of atmospheric braking to reach a bound orbit. In the current baseline, however, aerocapture is not used; instead, a purely propulsive capture and circularization sequence is executed to simplify thermal and structural design of the orbiter.

The modeled Mars-orbit insertion (MOI) sequence is:

- $\Delta v_1 = 0.000 \text{ km s}^{-1}$ — hyperbolic arrival to periapsis (no burn).
- $\Delta v_2 = 0.056 \text{ km s}^{-1}$ — small plane adjustment at apoapsis to align with the desired science-orbit inclination.
- $\Delta v_3 \approx 1.434 \text{ km s}^{-1}$ — distributed circularization burns near periapsis to achieve a $\sim 250 \text{ km}$ circular science orbit.

The circularization maneuver Δv_3 is implemented as a sequence of 49 short burns, each delivering $\sim 0.022\text{--}0.040 \text{ km s}^{-1}$ over 6 minutes. The total circularization time is 294 minutes, spread over multiple periapsis passages to manage thermal loads and allow navigation updates between burns. Including the plane-change maneuver to 120° degrees, the MONARC-445 stage delivers a total insertion Δv of

$$\Delta v_{MOI,\text{total}} = \Delta v_2 + \Delta v_3 \approx 1.490 \text{ km s}^{-1}. \quad (6)$$

The MONARC stage carries a design propellant load of $m_{prop,\text{design}} = 3,966 \text{ kg}$. The detailed burn ledger indicates that

$$m_{prop,\text{used}} \approx 3,564 \text{ kg}, \quad (7)$$

$$m_{prop,\text{rem}} \approx 402 \text{ kg}, \quad (8)$$

so that roughly 10.1% of the loaded propellant remains available after orbit circularization for trajectory trimming, attitude control, and end-of-life disposal.

Inverting the Tsiolkovsky rocket equation for the same $\Delta v_{MOI,\text{total}}$ and spacecraft dry mass yields an “optimal” propellant requirement of

$$m_{prop,\text{opt}} \approx 3,198 \text{ kg}, \quad (9)$$

implying that the current design carries approximately $m_{margin} \approx 768 \text{ kg}$ of propellant margin in the MONARC stage. This excess is intentional: it accommodates navigation dispersions, potential trajectory redesign (e.g., inclination changes to support alternate landing sites), and extended-mission operations, while also providing robustness against off-nominal I_{sp} or thrust performance.

Distributed Burn Strategy. The use of many short burns, rather than a single impulsive capture maneuver, offers several advantages:

- improved thermal management of the MONARC engine and associated structures;
- reduced peak thrust loads on the orbiter and probe attachment hardware;
- frequent opportunities for navigation updates and Δv trimming between burns;

- modest exploitation of the Oberth effect by concentrating Δv near periapsis.
- The penalty in operation time (a few hours spread over multiple orbits) is acceptable for a robotic mission and is outweighed by the improved controllability and fault tolerance.

Overall, the combined launch and insertion sequence yields an end-to-end mission Δv of

$$\Delta v_{\text{total}} = \Delta v_{\text{LEO} \rightarrow C_3} + \Delta v_{\text{MOI, total}} \approx 3.634 + 1.490 = 5.124 \text{ km s}^{-1}, \quad (10)$$

with propellant margins exceeding 20% at the launch-vehicle level and about 19% at the MONARC stage level (relative to the optimal requirement). This confirms that the MAGPIE configuration is comfortably compatible with a single Falcon 9 launch while preserving headroom for future growth in orbiter mass or additional payloads.

VI. Orbiter Design

The orbiter (also referred to as the orbiter module) is responsible for delivering the probe stack to Mars, deploying the probes into their EDL trajectories, and providing communications relay support throughout cruise and surface operations. Its design couples propulsion, attitude control, power, and communications subsystems with the needs of both the probes and the Deep Space Network (DSN) or future Mars relay infrastructure. The orbiter contains two observation cameras: one wide-angle and one narrow-angle. These cameras support probe-deployment verification, visual weather observation, and redundancy to other sensing systems. The Orbiter will have a parking orbit at Mars of an altitude of 350 km at a 120° degree inclination.

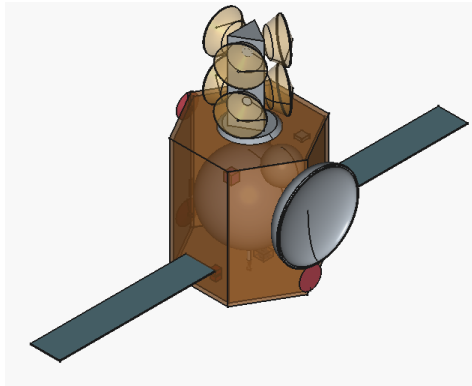
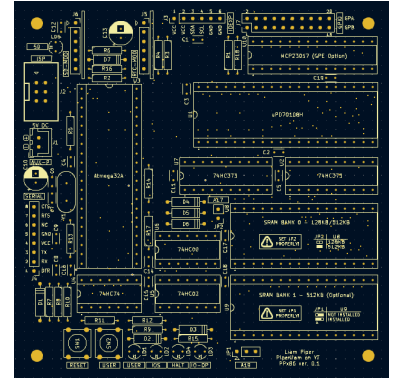


Fig. 4 Orbiter with Probes Integrated



safe-mode uses coarse sun sensors (CSS) and gyro propagation to keep the solar arrays illuminated and rates bounded while higher-performance sensors recover.

Architecture Overview. The GNC architecture can be summarized as:

- 1) **Sensing:** Dual star trackers (1–10 Hz), array-mounted CSS, tri-axial ADIS16470 IMU (200 Hz) providing body-frame rates and accelerations, tri-axial magnetometer for coarse detumble, and a side-looking optical imager capable of star-field attitude estimation.
- 2) **Estimation:** A 10-state multiplicative EKF over $(\mathbf{q}, \boldsymbol{\omega}, \mathbf{b}_g)$ with asynchronous updates from ST/CSS/CV, providing a continuous best estimate of attitude and body rates with gyro-bias tracking.
- 3) **Guidance:** Time-optimal bang–coast–bang slews for large reorientations, zero-rate pointing for science and relay, and sun-acquisition plus rate damping for safe mode.
- 4) **Control:** PD/LQR control on quaternion and rate error, with explicit torque and acceleration limiting, anti-windup, and jitter-filtering to protect structures and payloads.
- 5) **Actuation:** Three RW clusters (RW-A/B built from RW250 wheels, RW-C from RW25 wheels), plus monoprop RCS reserved for contingency detumble and wheel desaturation during rare off-nominal events.

Guidance provides reference attitudes or rates; control converts these into commanded body torques; allocation maps torques into individual wheel commands; estimation closes the loop by feeding back the best attitude/rate estimate to guidance and control.

Inertial measurement unit commonality. Both the orbiter and the MAGPIE probes baseline the same ADIS16470 tri-axial IMU module. Using a common inertial sensor across all vehicles simplifies calibration, dynamics modeling, and EKF tuning; the same bias and noise models can be applied to both the orbiter and probe GNC filters, and flight data from one element of the architecture directly informs the others. On the orbiter, the ADIS16470 operates continuously at 200 Hz and serves as the primary rate source for both high-accuracy attitude propagation and safe-mode rate damping.

State Estimation and Quaternion Filtering

Multiplicative EKF state and process model. The estimator state collects attitude, body rates, and gyro bias:

$$\mathbf{x} = \begin{bmatrix} \mathbf{q} \\ \boldsymbol{\omega} \\ \mathbf{b}_g \end{bmatrix}, \quad \tilde{\boldsymbol{\omega}} = \boldsymbol{\omega} + \mathbf{b}_g + \mathbf{n}_g,$$

where \mathbf{q} is the body-to-inertial quaternion, $\boldsymbol{\omega}$ the true body rate, \mathbf{b}_g the gyro bias, and $\tilde{\boldsymbol{\omega}}$ the measured gyro rate [4].

The continuous-time process model is

$$\dot{\mathbf{q}} = \frac{1}{2} \Omega(\tilde{\boldsymbol{\omega}} - \mathbf{b}_g) \mathbf{q}, \quad (11)$$

$$\mathbf{J}\dot{\boldsymbol{\omega}} = \boldsymbol{\tau}_c + \boldsymbol{\tau}_w - \boldsymbol{\omega} \times (\mathbf{J}\boldsymbol{\omega}) + \boldsymbol{\tau}_{dist}, \quad (12)$$

$$\dot{\mathbf{b}}_g = \mathbf{w}_b, \quad (13)$$

where \mathbf{J} is the spacecraft inertia, $\boldsymbol{\tau}_c$ is the commanded body torque, $\boldsymbol{\tau}_w$ is the wheel back-reaction, $\boldsymbol{\tau}_{dist}$ lumps disturbances (gravity-gradient, SRP, etc.), and \mathbf{w}_b is a small random-walk process that models gyro-bias drift.

In discrete time with step Δt , the EKF uses a numerical integrator (RK4) to propagate $\mathbf{x}_k^+ \mapsto \mathbf{x}_{k+1}^-$ and computes the state-transition Jacobian [4]

$$\mathbf{F}_k = \left. \frac{\partial f}{\partial \mathbf{x}} \right|_{\mathbf{x}_k^+},$$

to propagate the covariance:

$$\mathbf{P}_{k+1}^- = \mathbf{F}_k \mathbf{P}_k^+ \mathbf{F}_k^\top + \mathbf{Q}_k.$$

Measurement models. Star tracker, CV camera, and sun sensors provide attitude-related measurements at different cadences:

- **Star tracker (quaternion):**

$$\tilde{\mathbf{q}}^{(st)} = \mathbf{q} \otimes \delta\mathbf{q}_{st}, \quad \delta\mathbf{q}_{st} \approx \begin{bmatrix} 1 \\ \frac{1}{2}\theta_{st} \end{bmatrix},$$

where θ_{st} is a small zero-mean attitude error. The residual is computed as the small rotation that maps the predicted quaternion to the measured one.

- **Sun sensor (body-frame unit vector):**

$$\tilde{\mathbf{s}}_b = \mathbf{R}(\mathbf{q}) \mathbf{s}_I + \mathbf{n}_{sun},$$

where \mathbf{s}_I is the inertial Sun vector (from ephemerides) and $\mathbf{R}(\mathbf{q})$ is the DCM corresponding to \mathbf{q} . This provides a single vector constraint on attitude.

- **CV star tracker (quaternion, see below):**

$$\tilde{\mathbf{q}}^{(cv)} = \mathbf{q} \otimes \delta\mathbf{q}_{cv},$$

with larger covariance than the dedicated star tracker but identical measurement structure.

Each measurement provides a residual \mathbf{y}_k and Jacobian \mathbf{H}_k , which the EKF uses for the update:

$$\mathbf{K}_k = \mathbf{P}_k^- \mathbf{H}_k^\top (\mathbf{H}_k \mathbf{P}_k^- \mathbf{H}_k^\top + \mathbf{R}_k)^{-1}, \quad (14)$$

$$\delta\hat{\mathbf{x}}_k = \mathbf{K}_k \mathbf{y}_k, \quad (15)$$

$$\mathbf{x}_k^+ \leftarrow \text{boxplus}(\mathbf{x}_k^-, \delta\hat{\mathbf{x}}_k), \quad (16)$$

$$\mathbf{P}_k^+ = (\mathbf{I} - \mathbf{K}_k \mathbf{H}_k) \mathbf{P}_k^-. \quad (17)$$

The attitude part of $\delta\hat{\mathbf{x}}_k$ is converted into a small quaternion $\delta\mathbf{q}_k \approx [1, \frac{1}{2}\delta\theta_k]^\top$ and applied multiplicatively:

$$\mathbf{q}_k^+ = \delta\mathbf{q}_k \otimes \mathbf{q}_k^-,$$

which preserves unit norm and avoids the singularities of minimal-angle parameterizations [4].

Asynchronous updates are handled by running prediction steps at the IMU rate and applying each sensor update as its data arrive, with the measurement covariance \mathbf{R}_k tuned to reflect each sensor's accuracy.

Mathematical Formulation of CV Star-Tracking

When the primary star tracker is unavailable or degraded, the side-looking imager provides a reduced-accuracy, but still useful, attitude estimate. The CV pipeline converts a raw image (Fig. 6) into a quaternion and covariance in five steps:

- 1) Detect stars and compute their centroids
- 2) Convert centroids to unit vectors in the camera frame
- 3) Form geometric invariants and match them to a precomputed catalog
- 4) Solve Wahba's problem using QUEST to obtain the best-fit attitude
- 5) Estimate an attitude covariance for EKF fusion.

1. Image-plane star detection and centroiding. Let the imager produce a 2-D intensity array. Thresholding and non-maximum suppression identify star-like blobs; sub-pixel centroids in pixel coordinates are

$$\mathbf{p}_i = [u_i, v_i]^\top.$$

Using the calibrated intrinsics (f_x, f_y, c_x, c_y) , each centroid is mapped to a normalized direction in the camera frame:

$$x_i = \frac{u_i - c_x}{f_x}, \quad y_i = \frac{v_i - c_y}{f_y}, \quad \mathbf{v}_i = \frac{1}{\sqrt{x_i^2 + y_i^2 + 1}} \begin{bmatrix} x_i \\ y_i \\ 1 \end{bmatrix}.$$

Thus each detected star becomes a unit vector \mathbf{v}_i pointing from the camera center into the star field.



Fig. 6 Example star field from the orbiter’s side-looking camera used by the CV star-tracking mode. Detected stars (Green Markers) are matched to a reduced Tycho-2 catalog to recover the camera attitude when the primary star tracker is unavailable.

2. Geometric invariants (triangles or quads). To match observed stars to catalog stars without knowing attitude, the algorithm uses rotation-invariant features constructed from constellations of stars. For any triplet (i, j, k) , define side-length ratios

$$r_1 = \frac{\|\mathbf{v}_i - \mathbf{v}_j\|}{\|\mathbf{v}_i - \mathbf{v}_k\|}, \quad r_2 = \frac{\|\mathbf{v}_j - \mathbf{v}_k\|}{\|\mathbf{v}_i - \mathbf{v}_k\|}.$$

These ratios depend only on the *relative* geometry of the three stars, not on the overall orientation of the camera.

An equivalent, numerically stable representation uses angular separations

$$\theta_{ij} = \arccos(\mathbf{v}_i^\top \mathbf{v}_j),$$

and normalized invariants

$$\gamma_1 = \frac{\theta_{ij}}{\theta_{ik}}, \quad \gamma_2 = \frac{\theta_{jk}}{\theta_{ik}},$$

which are also invariant under rigid rotations.

3. Catalog pre-processing and matching. Offline, a subset of the Tycho-2 catalog is converted into inertial-frame unit vectors \mathbf{s}_ℓ and all admissible star triangles are enumerated. For each catalog triangle m the invariants $(r_1^{(m)}, r_2^{(m)})$ (or $(\gamma_1^{(m)}, \gamma_2^{(m)})$) and the corresponding star directions $\mathbf{s}_a^{(m)}, \mathbf{s}_b^{(m)}, \mathbf{s}_c^{(m)}$ are stored:

$$C = \{(r_1^{(m)}, r_2^{(m)}, \mathbf{s}_a^{(m)}, \mathbf{s}_b^{(m)}, \mathbf{s}_c^{(m)})\}.$$

A KD-tree indexed by (r_1, r_2) enables fast nearest-neighbor queries in invariant space.

On board, each observed triangle (i, j, k) yields invariants (r_1, r_2) . The KD-tree returns the closest catalog triangle(s), producing association hypotheses

$$\mathbf{v}_i \leftrightarrow \mathbf{s}_a, \quad \mathbf{v}_j \leftrightarrow \mathbf{s}_b, \quad \mathbf{v}_k \leftrightarrow \mathbf{s}_c.$$

Multiple triangles are considered; hypotheses that lead to consistent attitudes across triangles receive higher votes and survive to the next stage, while inconsistent ones are pruned.

4. Wahba's problem and QUEST solution. Once a set of N correspondences $(\mathbf{v}_i, \mathbf{s}_i)$ is assembled, the attitude is obtained by solving Wahba's problem:

$$\min_{\mathbf{R} \in SO(3)} J(\mathbf{R}) = \frac{1}{2} \sum_{i=1}^N w_i \|\mathbf{v}_i - \mathbf{R}\mathbf{s}_i\|^2,$$

where w_i are positive weights (e.g., based on brightness or centroid quality).

Define

$$B = \sum_i w_i \mathbf{v}_i \mathbf{s}_i^\top, \quad S = B + B^\top, \quad \sigma = \text{tr}(B), \quad \mathbf{z} = \sum_i w_i (\mathbf{v}_i \times \mathbf{s}_i).$$

Davenport's K -matrix is

$$K = \begin{bmatrix} S - \sigma I & \mathbf{z} \\ \mathbf{z}^\top & \sigma \end{bmatrix}.$$

The optimal attitude quaternion \mathbf{q}_{cv} is the normalized eigenvector corresponding to the maximum eigenvalue of K .

The QUEST algorithm avoids explicit eigen-decomposition by solving a scalar equation for the optimal eigenvalue λ_{opt} and then forming \mathbf{q}_{cv} from $(B, \mathbf{z}, \lambda_{\text{opt}})$. This reduces computation and is well-suited to flight processors.

5. Covariance generation and EKF fusion. To fuse the CV attitude estimate into the EKF, an approximate covariance must be assigned.

Assume pixel-level centroid noise with variances σ_u^2, σ_v^2 . Linearizing the pinhole projection, the covariance of each direction vector \mathbf{v}_i is

$$\mathbf{R}_{v,i} \approx \mathbf{J}_{proj,i} \begin{bmatrix} \sigma_u^2 & 0 \\ 0 & \sigma_v^2 \end{bmatrix} \mathbf{J}_{proj,i}^\top,$$

where $\mathbf{J}_{proj,i}$ is the Jacobian of the mapping $(u_i, v_i) \mapsto \mathbf{v}_i$.

Stacking the vector residuals for all stars, Wahba's problem can be written as

$$\mathbf{r}(\boldsymbol{\theta}) \approx \mathbf{H}\boldsymbol{\theta} + \mathbf{n},$$

where $\boldsymbol{\theta}$ is a small three-parameter attitude error and

$$\mathbf{H} = \begin{bmatrix} [\mathbf{v}_1]_\times \\ \vdots \\ [\mathbf{v}_N]_\times \end{bmatrix}$$

is built from the skew-symmetric matrices $[\mathbf{v}_i]_\times$. Under the usual linear least-squares assumptions, the attitude-error covariance is approximated by

$$\mathbf{P}_\theta \approx (\mathbf{H}^\top \mathbf{R}_v^{-1} \mathbf{H})^{-1},$$

where \mathbf{R}_v is the block-diagonal covariance of the stacked vector measurements.

The EKF then treats \mathbf{q}_{cv} exactly like a star-tracker quaternion, but with measurement covariance derived from \mathbf{P}_θ . In practice this places CV updates between CSS and full star tracker in the estimator's weighting, providing useful attitude knowledge with $\sim 0.05\text{--}0.2^\circ$ accuracy during safemode or star-tracker outages.

Quaternion Control and Wheel Allocation

Quaternion-error control and guidance interface. Guidance provides a commanded attitude $\mathbf{q}_{cmd}(t)$ and, for slews, possibly a commanded rate profile $\omega_{cmd}(t)$ (e.g., the bang-coast-bang rate). [17] The controller works with the quaternion error

$$\mathbf{q}_e = \mathbf{q}_{cmd} \otimes \mathbf{q}^{-1} = \begin{bmatrix} q_{e0} \\ \mathbf{q}_{ev} \end{bmatrix}, \quad \mathbf{e}_\theta = 2\mathbf{q}_{ev},$$

and rate error $\tilde{\omega} = \omega - \omega_{cmd}$.

A PD control law commands body torque:

$$\tau_c = \mathbf{K}_p \mathbf{e}_\theta - \mathbf{K}_d \tilde{\omega},$$

with gains chosen per axis based on inertia, desired bandwidth, and disturbance levels. For tight pointing or jitter shaping, the same structure can be obtained from an LQR design linearized about the identity attitude. [17]

Rate-limiting, saturation, and anti-windup. To respect wheel and structural limits, the commanded torque is saturated and rate-limited:

$$\|\tau_c\|_\infty \leq \tau_{\max}, \quad \|\dot{\omega}\|_\infty \leq \alpha_{\max}.$$

When saturation occurs, the effective torque differs from the “ideal” PD torque. An anti-windup or reference-governor scheme modifies \mathbf{e}_θ slightly so that the closed-loop system remains stable and does not integrate large attitude errors while torque is clamped.

Wheel allocation. Let $\mathbf{A} \in \mathbb{R}^{3 \times N}$ contain the unit spin axes of N wheels, and $\mathbf{J}_w = \text{diag}(J_{w,i})$ their inertias. The wheel acceleration vector $\dot{\omega}_w$ produces body torque

$$\tau_w = -\mathbf{A} \mathbf{J}_w \dot{\omega}_w.$$

The allocation problem is to choose $\dot{\omega}_w$ so that τ_w tracks τ_c while keeping each wheel within speed and acceleration limits. A weighted least-squares allocator solves

$$\dot{\omega}_w^\star = \arg \min_{\dot{\omega}_w} \|\mathbf{W}(\mathbf{A} \mathbf{J}_w \dot{\omega}_w + \tau_c)\|_2^2$$

subject to $|\dot{\omega}_{w,i}| \leq \dot{\omega}_{\max,i}$ and $|\omega_{w,i}| \leq \omega_{\max,i}$. In the unsaturated case this reduces to the familiar pseudoinverse solution; in the saturated case the allocator enforces priorities encoded in \mathbf{W} (e.g., preferring to use cooler or healthier wheels).

Reaction Wheel Hardware Capability

RW250 limits and cluster scaling. Each RW250 wheel provides

$$h_{w,\max} = 4.0 \text{ N m s}, \quad \tau_{w,\max} \approx 0.10 \text{ N m},$$

with ≤ 13 W of electrical power at high speed. The four-wheel skew cluster geometry means that, along any principal body axis, only some components of each wheel’s momentum and torque project onto that axis. Accounting for these projection factors and modest derating for thermal margins yields cluster-level per-axis limits

$$h_{\max}^{(A)} \approx 6\text{--}8 \text{ N m s}, \quad \tau_{\max}^{(A)} \approx 0.20\text{--}0.30 \text{ N m}.$$

With two clusters (RW-A and RW-B) operating together,

$$h_{\max}^{(A+B)} \approx 12\text{--}16 \text{ N m s}, \quad \tau_{\max}^{(A+B)} \approx 0.4\text{--}0.6 \text{ N m},$$

allowing significantly faster slews at the cost of higher average power and thermal loading.

Rate and acceleration bounds from hardware. For principal inertias $\mathbf{J} = \text{diag}(J_x, J_y, J_z)$, the wheel limits define maximum body rates and accelerations:

$$\omega_{\max,i} = \frac{h_{\max,i}}{J_i}, \quad \alpha_{\max,i} = \frac{\tau_{\max,i}}{J_i}.$$

These bounds are used by guidance when designing bang–coast–bang slews, by control when selecting gains (bandwidth cannot exceed α_{\max} by a large factor), and by operations to ensure that commanded maneuvers remain within mechanical and thermal envelopes.

Large-Angle Slew Dynamics

Observed envelope and comparison to analytic bounds. Closed-loop simulations with a single RW250 cluster and gains $K_p = 0.2$, $K_d = 25$ show that slews of 5–180° about any principal axis all converge in roughly

$$t_{\text{settle}} \approx 1800\text{--}2000 \text{ s},$$

with peak body rates

$$|\omega|_{\max} \approx 0.45\text{--}0.46^\circ/\text{s}.$$

These values match the hardware-derived rate limits $\omega_{\max,i}$, confirming that the slews are rate-limited rather than gain-limited: once the spacecraft hits its allowed rate, the controller holds that rate until it is time to brake. [17]

Energy cost and power profile. The total reaction-wheel electrical energy for a slew is

$$E_{\text{RW}} = \int_0^T P_{\text{RW}}(t) dt,$$

where $P_{\text{RW}}(t)$ includes both mechanical spin-up power and losses. Because each slew consists of a spin-up phase, a nearly constant-speed coast, and a symmetric spin-down, the energy is dominated by the two spin transients and is almost independent of commanded angle:

$$E_X \approx 0.21 \text{ Wh}, \quad E_Y \approx 0.16 \text{ Wh}, \quad E_Z \approx 0.30 \text{ Wh}.$$

Peak power is in the 1–25 W range depending on axis and angle; average power E_{RW}/T remains below 0.6 W.

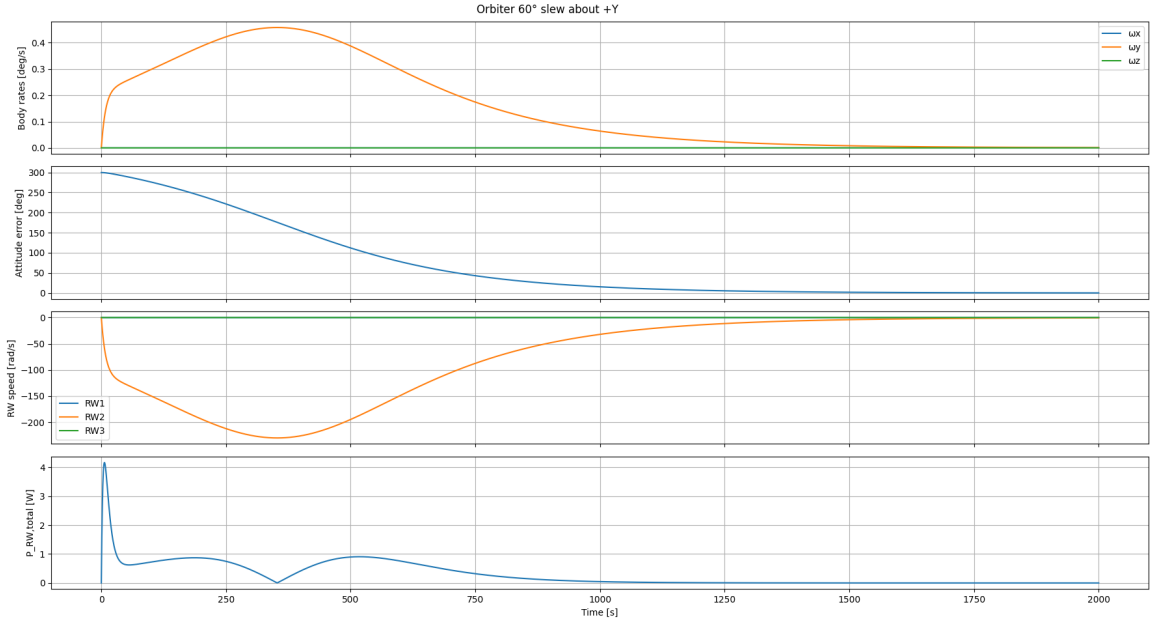


Fig. 7 Closed-loop 60° slew about body +Y. Top: body rates saturate at the hardware-derived rate limit. Middle: attitude error decays monotonically. Bottom: wheel speeds and total electrical power show the expected bang–coast–bang structure.

These values show that even large reorientations consume only a few tenths of a watt-hour, making frequent slews energetically acceptable.

Nadir-Hold Dynamics vs Orbit Altitude

Orbital-rate requirement. For a circular Mars orbit with radius $r = R_M + h$, the orbital rate is

$$\omega_o(h) = \sqrt{\frac{\mu_M}{r^3}}.$$

Table 6 Orbiter RW250 slew performance (body Y axis, single RW250 cluster).

Angle	t_{settle} [s]	$ \omega _{\text{max}}$ [deg/s]	E [Wh]	\bar{P} [W]	P_{max} [W]
5	2000	0.458	0.160	0.289	0.91
30	1958	0.458	0.160	0.289	1.12
60	1917	0.458	0.160	0.289	4.16
90	1879	0.458	0.160	0.289	8.30
180	1767	0.453	0.157	0.282	16.35

For $h = 250\text{--}1000$ km this evaluates to

$$\omega_o \approx 0.572^\circ/\text{s},$$

which is the rate at which the nadir vector rotates in inertial space. To keep instruments pointed at nadir, the reaction wheels must spin such that the spacecraft body tracks this rotation continuously. [17]

Daily energy cost. Simulations compute the torque and wheel speeds required to track ω_o over one orbit, yielding an orbital energy $E_{\text{orbit}}(h)$ and, by scaling with the number of orbits per sol, a daily energy cost

$$E_{\text{sol}}(h) = \frac{T_{\text{sol}}}{T_{\text{orbit}}(h)} E_{\text{orbit}}(h).$$

For the three representative altitudes,

$$\bar{P}_{RW} \approx 1.1\text{--}1.4 \text{ W}, \quad E_{\text{sol}} \approx 27\text{--}36 \text{ Wh},$$

with only weak dependence on altitude.

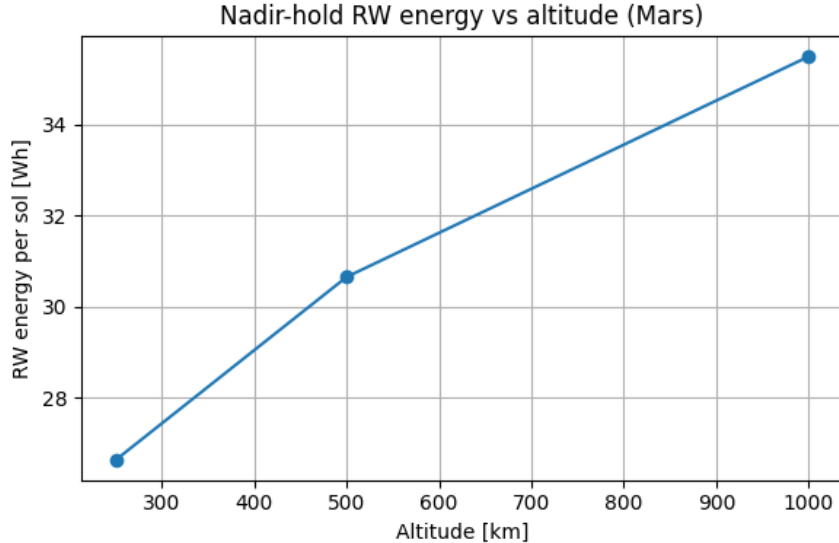


Fig. 8 Average reaction-wheel power required for continuous nadir pointing vs circular orbit altitude.

These numbers set the “standing cost” of keeping the orbiter in science/relay pointing; they are small compared to the available solar power, leaving margin for payload, thermal control, and communications.

Momentum Management (Propellantless)

Wheel momentum accumulates under constant disturbances according to

$$\dot{\mathbf{h}}_w = -\boldsymbol{\tau}_{\text{dist}},$$

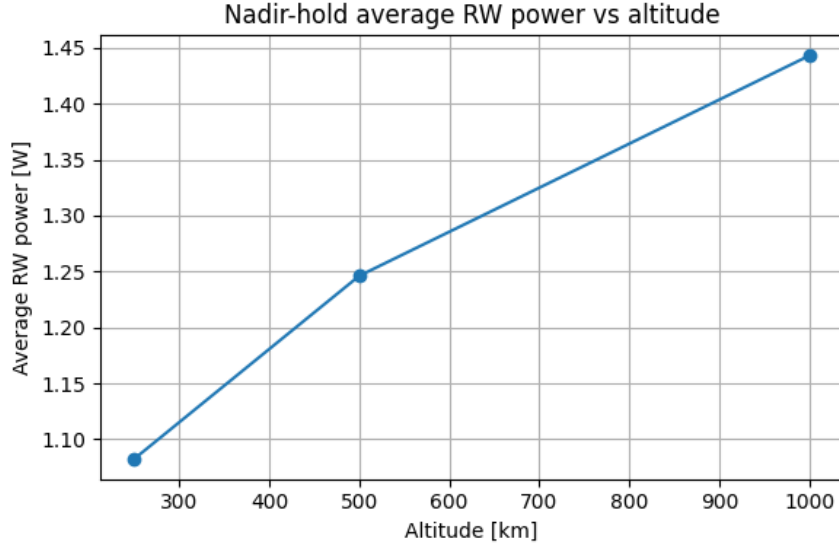


Fig. 9 Total reaction-wheel energy per sol during nadir pointing vs orbit altitude.

where τ_{dist} includes gravity-gradient and solar radiation pressure torques. For gravity-gradient about axis i ,

$$\tau_{gg,i} = 3\omega_o^2(J_j - J_k) \sin \phi \cos \phi,$$

with ϕ the angle between the i -axis and the local vertical.

A simple upper bound on total wheel momentum is h_{\max} . Unload triggers at

$$\|\mathbf{h}_w\| > \eta h_{\max}, \quad \eta = 0.7\text{--}0.85,$$

at which point the guidance layer inserts a small attitude bias $\Delta\mathbf{e}_\theta$ that increases the projection of τ_{dist} onto \mathbf{h}_w :

$$\max_{\Delta\mathbf{e}_\theta} \int_0^{T_b} \hat{\mathbf{h}}_w^\top \tau_{dist}(\mathbf{q}(t; \Delta\mathbf{e}_\theta)) dt,$$

subject to pointing keep-outs and thermal limits. During this short bias, environmental torques drive wheel speeds back toward zero, reducing stored momentum without expending propellant.

Probe RW25 Performance (Comparison)

For context, a single MAGPIE probe uses a single RW25 wheel for minor attitude trims and relay pointing. Simulations for the probe inertia show

$$|\omega|_{\max} \approx 0.048^\circ/\text{s}, \quad E_{\text{slew}} \approx 0.0045 \text{ Wh},$$

with peak power below 2 W. Thus, probe attitude operations are negligible in their energy budgets and provide a convenient check on the RW modeling used for the orbiter.

Mission Duration and Modes. The orbiter ADCS remains active across cruise, MOI, and the ~28-sol probe campaign. Mode logic prioritizes:

- 1) sun-acquisition and rate damping (Safe mode),
- 2) momentum unloading if wheel storage approaches limits,
- 3) fine pointing for science and relay, and
- 4) large-angle slews for viewing geometry changes and HGA tracking.

The combination of analytic bounds, detailed simulations, and CV-based contingency sensing shows that pointing, slew, and nadir-hold requirements can be met with comfortable power and thermal margins for the full mission duration.

B. Orbiter Electrical Power System

The MAGPIE orbiter uses a conventional solar-array–battery power system with a regulated 28 V bus, maximum power point tracking (MPPT) on each array string, and a NiMH battery pack sized to ride through eclipse and high-power downlink events. In keeping with the probe architecture, NiMH chemistry is selected for its benign failure modes, radiation tolerance, and heritage in cold planetary environments, at the cost of lower specific energy relative to Li-ion [4].

1. Architecture Overview

The EPS comprises:

- A deployable solar array with a nameplate capacity of 900 W at Mars distance;
- Dual-redundant MPPT converters, each fed by a pair of wings, feeding the 28 V bus;
- A 28 V NiMH battery pack with nominal energy capacity $C_{\text{batt}} = 950 \text{ Wh}$ ($\sim 110 \text{ Ah}$) and cell-level monitoring;
- A redundant power control and distribution unit (PCDU) that implements bus regulation, battery charge control, and prioritized load shedding.

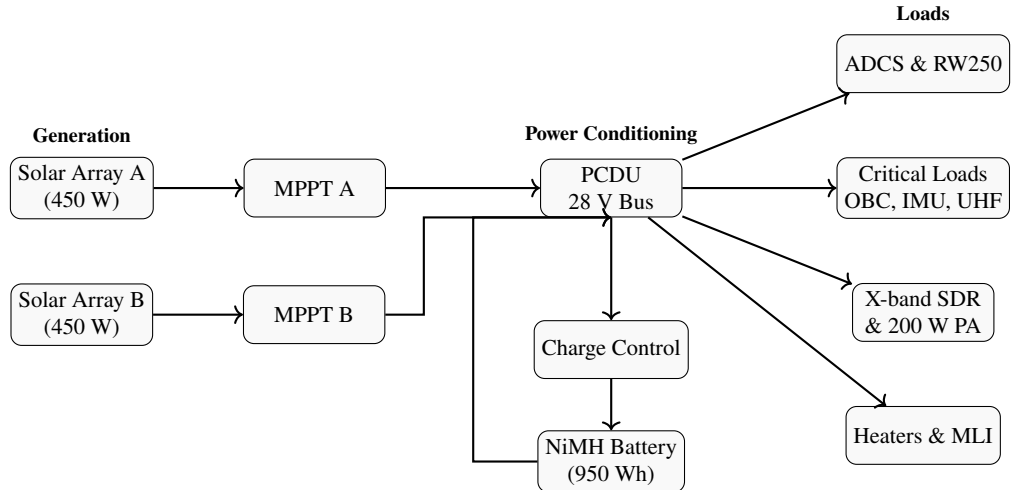


Fig. 10 MAGPIE Orbiter EPS flow diagram. Dual MPPT converters feed a regulated 28 V bus. A 950 Wh NiMH battery provides storage with controlled charge/discharge paths. The PCDU distributes power to ADCS, avionics, communications, and thermal control subsystems.

Figure 10 shows the high-level EPS architecture. The solar arrays are operated at their instantaneous maximum power point by dedicated MPPT converters, which decouple array I–V behaviour from the bus voltage and battery state of charge. The PCDU regulates the 28 V main bus, routes power to essential and non-essential loads, and enforces under-voltage lockout and staged load shedding in contingency modes.

2. Array and Battery Sizing

At Mars, the mean solar irradiance is

$$G_{\text{Mars}} = \frac{G_{1\text{AU}}}{r_{\text{Mars}}^2} \approx \frac{1361 \text{ W/m}^2}{1.52^2} \approx 589 \text{ W/m}^2, \quad (18)$$

where $G_{1\text{AU}}$ is the solar constant and r_{Mars} is Mars' heliocentric distance in AU. For an assumed cell efficiency $\eta_{\text{panel}} = 0.29$, the required deployed area to achieve 900 W nameplate power at Mars is [4]

$$A_{\text{sa}} = \frac{P_{\text{rated}}}{\eta_{\text{panel}} G_{\text{Mars}}} = \frac{900 \text{ W}}{0.29 \times 589 \text{ W/m}^2} \approx 5.27 \text{ m}^2. \quad (19)$$

In operation, array output is reduced by cell degradation due to radiation and off-normal pointing. These effects are modeled with multiplicative factors η_{rad} and η_{angle} , yielding an effective sunlit generation

$$P_{\text{sa,eff}} = P_{\text{rated}} \eta_{\text{rad}} \eta_{\text{angle}}, \quad (20)$$

with $\eta_{\text{rad}} = 0.85$ and $\eta_{\text{angle}} = 0.85$. For MAGPIE this gives

$$P_{\text{sa,eff}} = 900 \times 0.85 \times 0.85 \approx 650 \text{ W} \quad (21)$$

during the illuminated portion of the orbit.

The reference relay orbit has period $T_{\text{orb}} = 2.10 \text{ h}$ with an eclipse fraction of 33%, so that

$$t_{\text{sun}} \approx 1.41 \text{ h}, \quad (22)$$

$$t_{\text{ecl}} \approx 0.69 \text{ h}. \quad (23)$$

Using representative “alternate power” loads consistent with the communications and ADCS design— $P_{\text{day}} = 355 \text{ W}$ during sunlit segments and $P_{\text{ecl}} = 275 \text{ W}$ during eclipse—the per-orbit energy balance is

$$E_{\text{gen}} = P_{\text{sa,eff}} t_{\text{sun}} \approx 0.92 \text{ kWh}, \quad (24)$$

$$E_{\text{load}} = P_{\text{day}} t_{\text{sun}} + P_{\text{ecl}} t_{\text{ecl}} \approx 0.69 \text{ kWh}, \quad (25)$$

leaving a nominal surplus of $\sim 0.23 \text{ kWh}$ per orbit to recharge the battery and cover modelling uncertainties [4].

3. State-of-Charge Evolution

For system-level analysis, the battery state-of-charge (SOC) is propagated using a simple coulomb-counting model with an effective round-trip efficiency η_{rt} :

$$\text{SOC}_{k+1} = \text{SOC}_k + \frac{(P_{\text{sa}} - P_{\text{load}}) \Delta t}{C_{\text{batt}} \eta_{\text{rt}}}, \quad (26)$$

where $C_{\text{batt}} = 950 \text{ Wh}$ is the nominal energy capacity, P_{sa} and P_{load} are the instantaneous generation and load powers, and Δt is the integration timestep. A round-trip efficiency of $\eta_{\text{rt}} = 0.75$ is used to lump NiMH charge inefficiency and conversion losses. When $P_{\text{sa}} > P_{\text{load}}$, the SOC increases up to a ceiling of 100%; when $P_{\text{sa}} < P_{\text{load}}$, the difference is drawn from the battery until a lower bound (20% SOC) triggers load shedding or safe mode.

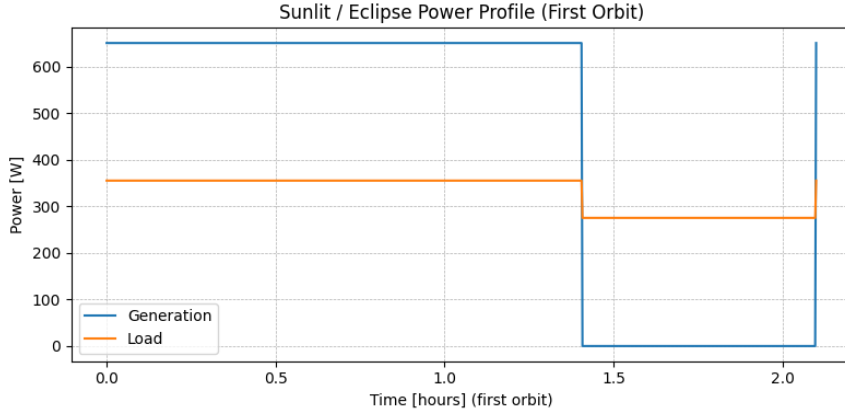


Fig. 11 Orbiter module array power generation.

A 40-orbit simulation (84 h) with initial SOC = 80% shows that the pack remains comfortably above the lower limit for the entire run, with

$$\text{SOC}_{\min} \approx 80\%, \quad (27)$$

$$\text{SOC}_{\text{final}} \approx 91.5\%. \quad (28)$$

The SOC floor is never reached, indicating that the 950 Wh NiMH pack provides substantial margin for extended downlink passes, elevated heater duty cycles, or moderate radiation-induced array degradation. Figure 12 illustrates the SOC evolution over the 40-orbit case, highlighting the small depth-of-discharge (a few percent per orbit) that underpins long-term battery life [4].

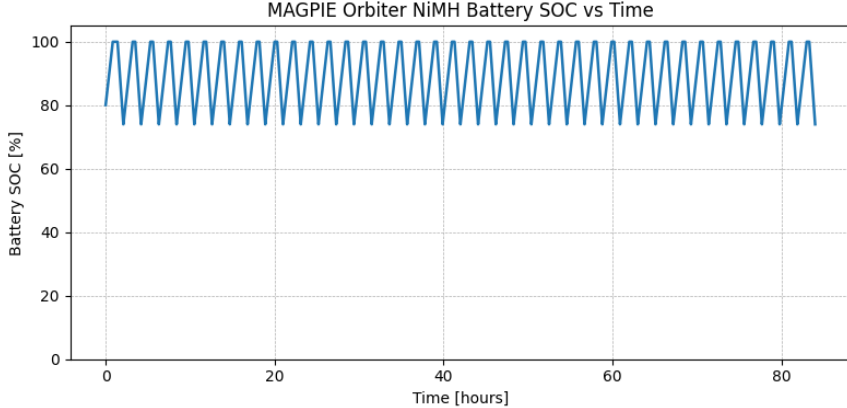


Fig. 12 Orbiter module state of charge (battery starting at 80%).

C. Orbiter Communications

Because one of the primary roles of the orbiter is data relay, the communications subsystem is critical to mission success. The orbiter carries a suite of antennas tailored to different downlink and relay modes: a high-gain and a low-gain dish for deep-space downlink, plus a helical, patch, and monopole antenna for UHF/ISM-band links to the probes. The dish antennas may also be cross-utilized for near-field relay when probe geometry allows line of sight.

The X-band communications chain supports both forward (command) and return (telemetry and science) links through the Deep Space Network (DSN). Each RF path is implemented using software-defined radios (SDRs) capable of adaptive modulation, coding, and carrier tracking. A 200 W class-E RF power amplifier is used for primary deep-space downlink, with a fully redundant bypass mode that routes the SDR directly to the feed for reduced-power emergency operation (~ 5 W transmit). This dual-path design ensures continued communications in the event of an amplifier or thermal-control failure.

Link-Budget Formulation. The received carrier power at Earth is given by the standard Friis transmission equation [18]:

$$P_r = P_t + G_t + G_r - L_p - L_s - L_a, \quad (29)$$

where P_t is transmit power (dBW), G_t and G_r are the transmitter and receiver antenna gains (dBi), L_p is free-space path loss (dB), L_s represents system losses (e.g., pointing and polarization), and L_a accounts for atmospheric attenuation. The free-space path loss is expressed as [18]

$$L_p = 92.45 + 20 \log_{10}(R) + 20 \log_{10}(f), \quad (30)$$

with R in kilometers and f in GHz.

The link margin M is then

$$M = P_r - (N_0 + 10 \log_{10}(B) + \text{Eb}/\text{N}_0\text{req}), \quad (31)$$

where $N_0 = 10 \log_{10}(kT_s)$ is the receiver noise spectral density, B the bandwidth, and $\text{Eb}/\text{N}_0\text{req}$ the minimum bit-energy-to-noise ratio for the selected modulation and coding scheme.

For the MAGPIE X-band link ($f = 8.4$ GHz) and a DSN 34 m Earth antenna ($G_r = 74.0$ dBi, $T_s = 20$ K), link margins were evaluated for various orbiter dish diameters and for both average ($R = 1.5$ AU) and worst-case opposition ($R = 2.5$ AU) geometries. The results are summarized in Figs. 13 and 14.

Performance and Data Modes. The modeled link margin at 200 W transmit power exceeds 40 dB for a 2 m high-gain dish at average range, and remains above 30 dB even at opposition. In low-power (amplifier-bypass) mode, the link margin falls to ~ 10 –12 dB but is still sufficient for low-rate telemetry (1–2 kbps) using robust coding [18].

Typical operational modes are summarized in Table 7. Mode 1 is used for primary science data downlink during DSN contact; Mode 2 provides low-rate housekeeping and command capability when operating on bypass power; and Mode 3 supports UHF relay to surface probes.

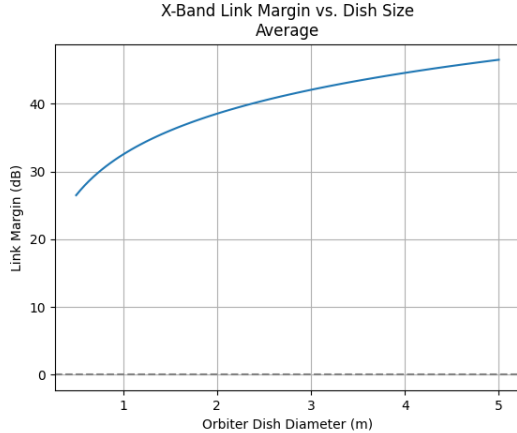


Fig. 13 X-band link margin vs. dish size at average Earth–Mars distance (1.5 AU).

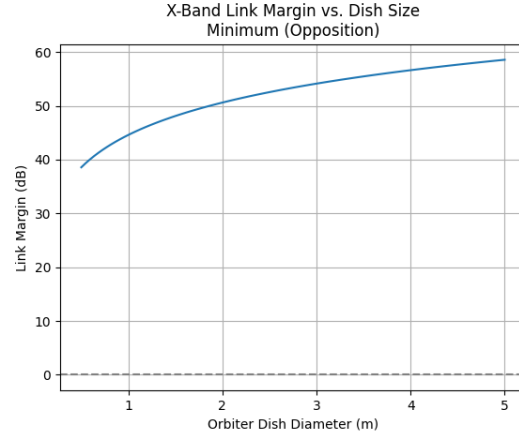


Fig. 14 X-band link margin vs. dish size at Mars opposition (2.5 AU).

Table 7 Nominal Communications Modes and Performance

Mode	Link Type	RF Power (W)	Data Rate (kbps)	Use Case
1	X-band (HGA)	200	256–1024	DSN science downlink
2	X-band (HGA, bypass)	5	1–8	Safe mode / telemetry
3	UHF relay (monopole/patch)	1	16–128	Probe relay link
4	ISM band (LoRa backup)	1	< 1	Redundant probe link

Antenna Selection. Using the link-margin curves, a 2.0 m deployable high-gain antenna (HGA) was selected as the baseline for deep-space communication. This provides ~42 dB of margin at average Earth–Mars range and ~34 dB at opposition, assuming 200 W transmit power and 34 m DSN reception. Three 0.25 m fixed low-gain dishes (LGA) provide omnidirectional coverage during safe-mode or cruise-phase operations when attitude knowledge is degraded.

For UHF proximity links to the distributed probes, the orbiter carries a 70 cm (433 MHz) dipole mounted over a planar flat reflector. The reflector increases the dipole’s broadside gain from ~2.1 dBi to ~5 dBi while improving front-to-back isolation. A flat reflector is preferred over a curved or parabolic geometry, as it maintains a wide beamwidth suitable for nadir relay passes and avoids the mechanical complexity of shaped surfaces. This configuration provides enhanced UHF reception and transmission performance without requiring precision pointing during overflights. With this gain and a minimum elevation angle of 20°, the UHF link maintains positive margin for all six probes throughout each overpass, supporting the required burst data return during the orbiter’s once-per-sol relay window.

Table 8 Antenna Gain Comparison

Antenna	433 MHz	915 MHz	X-band (8.4 GHz)
2.0 m Dish	16.9 dBi	23.4 dBi	42.7 dBi
0.25 m Dish	-1.1 dBi	5.4 dBi	24.6 dBi
Dual 0.25 m Dish	1.9 dBi	8.4 dBi	27.6 dBi
70 cm Dipole + Flat Reflector	5.0 dBi	–	–

The resulting UHF antenna gain, combined with the probe transmitters’ 1–3 W output and the orbiter’s low system noise temperature, yields more than sufficient link margin for reliable data extraction during each relay pass, ensuring full recovery of the probe science and housekeeping data once per sol.

The combination of SDR-based radios, redundant amplifier paths, and multi-band antennas ensures that the communications subsystem can sustain mission operations across a wide range of contingencies, from full-rate science transmission to minimal beacon telemetry.

D. Orbiter Propulsion

The MAGPIE orbiter employs a compact, storable monopropellant propulsion system centered around the MONARC-1 hydrazine thruster. Each engine provides approximately 445 N of nominal thrust through catalytic decomposition of hydrazine, fed from a single spherical propellant tank pressurized with regulated helium gas [19]. Because the system uses a single storable propellant, it requires no cryogenic conditioning and remains stable over multi-year cruise durations.

Design Overview. The propulsion module is mounted on the aft deck of the orbiter and consists of:

- A single spherical hydrazine propellant tank,
- A spherical high-pressure helium pressurant tank,
- Pressure regulators, check valves, and isolation valves,
- One MONARC-1 thruster arranged in a symmetric cluster,
- Thermally conditioned feed lines and heater circuits.

The hydrazine tank is mechanically integrated into the primary load path around the central avionics vault, minimizing center-of-mass migration as propellant is consumed. Small line heaters maintain hydrazine temperature above its freezing point during eclipses.

The propulsion subsystem supports:

- 1) Mars Orbit Insertion (MOI) using a distributed-burn sequence,
- 2) mid-course trajectory correction maneuvers,
- 3) attitude control support during probe deployment,
- 4) controlled deorbit or disposal at end of mission.

Performance Summary. Table 9 summarizes the propulsion performance across all MOI and trim burns.

Table 9 Hydrazine Propulsion System Performance Summary

Parameter	Symbol	Value	Unit
Number of thruster(s)	N_{eng}	1	–
Nominal thrust (each)	F	445	N
Specific impulse (vacuum)	I_{sp}	220	s
Propellant type	–	Hydrazine (monopropellant)	–
Propellant load (design)	$m_{\text{prop,design}}$	3966	kg
Propellant used (actual)	$m_{\text{prop,used}}$	3564	kg
Propellant remaining	$m_{\text{prop,rem}}$	402	kg (10.1%)
Total Δv delivered	Δv_{total}	1.490	km/s
Number of MOI burns	N_{burn}	49	–
Average burn duration	t_{burn}	6.0	min
Total burn time	t_{total}	294	min
Dry mass (orbiter bus)	m_{dry}	3519	kg

Operational Concept. During Mars arrival, the propulsion system performs a sequence of short, periapsis-centered burns. This approach:

- reduces thermal stress on catalytic beds,
- enables navigation updates between burns,
- provides distributed Δv delivery to refine the capture orbit.

Between major burns, the thrusters operate in pulse-mode for trajectory trimming and coarse attitude maneuvers. The plumbing architecture permits isolation of each thruster independently [4].

Subsystem Mass Breakdown.

Table 10 Propulsion Subsystem Mass Breakdown

Component	Mass (kg)	Fraction of Dry Mass (%)
Spherical hydrazine tank	510	39.8
MONARC-1 thruster	1.14	0.09
Feed lines, valves, regulators	44	3.43
Helium pressurant tank + COPV	585	45.6
Thermal and insulation hardware	28	2.2
Propulsion control electronics	10	0.78
Structural mounts, brackets	105	8.19
Total (dry)	1283	100

E. Orbiter Propellant Tank and Pressurization System

The MAGPIE orbiter uses two spherical tanks: a hydrazine propellant tank and a high-pressure helium pressurant tank. The tanks supply the MONARC-1 thruster during the 49-burn distributed Mars Orbit Insertion (MOI) sequence.

1. Propellant Volume

The total hydrazine load is:

$$m_{\text{hyd}} = 3966 \text{ kg}$$

Using the density of hydrazine, $\rho_{\text{hyd}} = 1010 \text{ kg/m}^3$,

$$V_{\text{hyd}} = \frac{m_{\text{hyd}}}{\rho_{\text{hyd}}} = 3.93 \text{ m}^3$$

Including 15% ullage and PMD volume [20]:

$$V_{\text{tank}} = 1.15 V_{\text{hyd}} = 4.52 \text{ m}^3$$

2. Tank Geometry and Structural Sizing

The hydrazine tank is a thin-walled spherical COPV with an aluminum liner. Tank volume is:

$$V = \frac{4}{3}\pi r^3$$

A representative solution is:

$$r = 1.01 \text{ m}$$

Hoop stress for a spherical vessel:

$$\sigma = \frac{p r}{2t}$$

Using $p = 2.2 \text{ MPa}$, allowable stress 250 MPa , and SF = 1.5 [20]:

$$t_{\min} = 6.6 \text{ mm}$$

3. Helium Pressurization System

Helium is stored in a spherical COPV at:

$$p_0 = 31 \text{ MPa}$$

For regulated feed pressure and full tank blowdown, required helium mass is:

$$m_{\text{He}} = \frac{p_0 V_{\text{tank}}}{R_{\text{He}} T} \approx 5\text{--}6 \text{ kg}$$

A single 0.05 m³ pressurant sphere satisfies the requirement with margin.

4. Propellant Management

The hydrazine tank includes:

- Vaned PMDs for vapor-free delivery
- Internal slosh baffles
- MLI and thermal straps for uniform temperature
- Line heaters for freeze protection.

5. Integration with Orbiter Structure

The hydrazine and helium spheres mount symmetrically around a central triangular retaining structure, minimizing center-of-mass migration around X–Y axis. This configuration closes mass, thermal, and structural margins for the 1.49 km/s MOI sequence with greater than 10% propellant reserve.

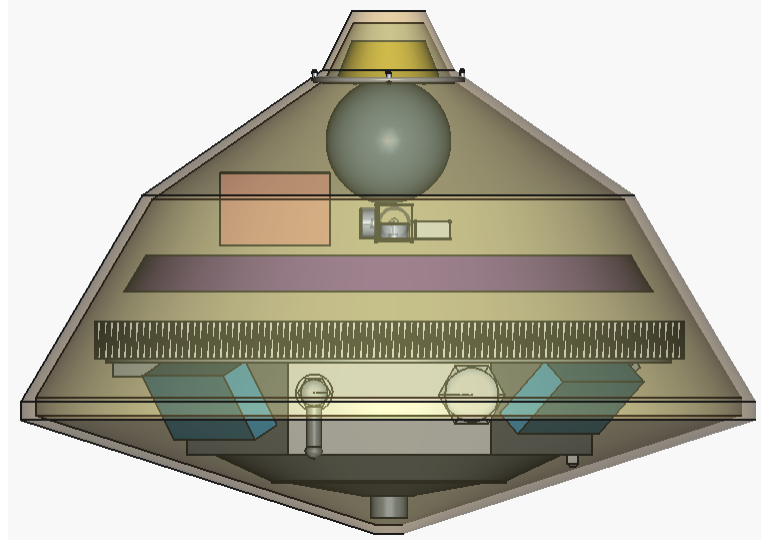


Fig. 15 Sidecut of Probe and Aeroshell with all components and sub-systems shown. This includes; OBC, Entire EDL System, Probe itself and internal design.

VII. Probe Design

Because the probes are the basis of the mission, they must be capable of landing at a wide range of sites on the Martian surface and surviving long enough to return useful scientific data. This requirement is especially challenging at high latitudes and during seasons when solar flux is low or highly variable.

A. General Overview

Each of the six probes has a mass of approximately 23 kg. Every probe includes its own EDL system, consisting of an aeroshell/heat shield and a small retrograde propulsion package. The probes operate entirely autonomously during cruise and EDL but can be commanded into a supervised or manual control mode for troubleshooting or targeted observation campaigns after landing.

The design of the probe is inspired in part by the Deep Space 2 mission, which flew two microprobes as part of the Mars Surveyor '98 program. Although those probes did not return data, the lessons learned from their design, qualification, and suspected failure modes directly inform MAGPIE [21]. In particular, MAGPIE adopts a more conservative entry environment, increased structural margins, improved communications links, and a power system sized for extended surface operations rather than brief impact experiments.

B. Probe Electronic Systems

The probe's electronic architecture balances performance, redundancy, and radiation tolerance within a strict microprobe mass and power envelope. The primary computing subsystem is built around a pair of cross-strapped Microchip SAMA7G54 with ARM Cortex-A7 processors running at up to 1 GHz. Each unit maintains synchronized execution of the same GNC, sequencing, and data-handling tasks; periodic state comparisons identify faults, allowing the healthy processor to take exclusive control. A physically independent RP2040 controller supervises both primaries, monitors heartbeats of the probe, arbitrates disagreements between the dual main OBC, and can assume autonomous control of heaters, power buses, and a low-rate emergency beacon if both main processors degrade. This tertiary controller is powered from a diode-isolated rail and boots from a minimal, radiation-tolerant ROM image.

Sensor and actuator interfaces are simplified into two fault-tolerant buses—a high-speed SPI⁴ cluster for the IMU, altimeter, and sun sensors, and an I²C backbone for thermal and housekeeping telemetry. A dedicated MIPI-CSI interface links the descent imager directly to the SAMA7G54's built-in ISP for onboard image compression. This bus architecture minimizes connector count, supports graceful degradation, and limits the blast radius of partial sensor failures.

Memory uses dual 128 GB industrial eMMC devices and 8 GB of ECC-enabled DDR4. Three independent partitions

store the primary image, fallback image, and a read-only golden configuration. All executable files are checked with CRC-32 before use, and the bootloader automatically falls back to the golden partition when verification fails. Periodic memory scrubbing reduces the impact of SEUs accumulated over long surface operations.

The avionics stack is mounted to an aluminum frame acting as both a structural support and heat spreader. Grapho-polymer thermal interfaces couple the SAMA7G54 directly to the probe chassis, allowing processor waste heat to contribute to nighttime thermal survival. Heaters are duty-cycled by the safing controller using redundant temperature sensors mounted near the battery and MPU cluster.

Radiation design assumptions follow a conservative Mars-surface model with a TID of 20–30 krad(Si) behind 2.5 mm aluminum equivalent over a three-year mission. Electronics are enclosed within a compact radiation vault providing localized shielding around the SAMA7G54, DDR memory, and eMMC. Additional mitigation includes conformal coating, current limiting on all external interfaces, SEU-resistant firmware on the safing controller, and architectural redundancy that prevents any single event from producing a mission-ending state.

Fault management is handled through a three-tier system: (i) hardware brownout, overcurrent, and bus-reset logic; (ii) cross-comparison and demotion of failing MPUs; and (iii) takeover by the RP2040 safing controller, which can enter a cold-survival mode, shed loads, reconfigure radios, and maintain beaconing. This ensures that even under partial degradation, the probe retains the ability to relay science data and health telemetry.

Table 11 Condensed Failure Mode and Effects Analysis (FMEA) for Probe Electronics

Subsystem	Failure Mode	Effect	Mitigation
Primary SAMA7G54	SEU, latchup, or reset	Loss of one processor; transient loss of compute margin	Current limiting, automatic power-cycle, rapid failover to redundant MPU.
Redundant MPU pair	Disagreement or divergent states	Commands blocked; system enters hold state	Safing MCU arbitrates, demotes bad node, promotes good node.
Safing MCU (RP2040)	Watchdog / firmware upset	Loss of autonomous recovery logic	ROM-based fallback image; hardware watchdog and brownout reset.
IMU / GNC sensors	Bias jump or lockup	Reduced attitude knowledge	EKF gating, sensor voting, fallback to coarse sun sensors.
eMMC / DDR memory	Bit errors, corrupted sectors	Boot failure or data loss	Triple-partition images, ECC, CRC-verified boot, golden fallback.
Power regulation	Over/undervoltage or latchup	Unexpected resets; possible IC stress	Redundant regulators, OVP, current limiting, safing-controlled load shedding.
Board interconnects	Open/short on SPI/I ² C	Loss of sensor channel; potential bus freeze	Segmented buses, pull-ups, firmware resets, cross-strapped critical sensors.
Thermal control	Heater or sensor fault	Overheating or cold-soak	Redundant thermistors, safing-enforced limits, conservative heater profiles.

Summary. Through a combination of dual SAMA7G54 processors, an independent safing controller, radiation-tolerant packaging, robust memory protection, and structured fault-management, the MAGPIE probe avionics provide a compact yet highly resilient computing platform capable of maintaining science return even under partial failures or radiation-induced degradation.

1. Communications System

Each MAGPIE probe incorporates a fault-tolerant, multi-band communications subsystem designed to ensure reliable data return throughout cruise, entry–descent–landing (EDL), and the full duration of surface operations. The architecture employs deliberate redundancy in *frequency*, *antenna geometry*, and *polarization*, thereby maintaining link closure under adverse probe attitudes, terrain shadowing, or elevated atmospheric dust loading.

Two independent radios provide dual-path communications capability:

- A **433 MHz UHF transceiver** (3–5 W RF), serving as the primary deep-surface relay link.
- A **915 MHz LoRa transceiver** (3 W RF), supplying an ISM-band channel with adaptive data rates and robust forward-error correction.

Both transceivers interface through a unified command/data bus, enabling either radio to support scheduled orbiter passes or serve as a cross-check during commissioning and health assessment.

Antenna Suite Overview. To enhance robustness across the full range of probe attitudes and environmental conditions, the communications subsystem employs three different complementary antennas with distinct radiation patterns and polarizations:

- 1) **Primary Antenna — 433 MHz Quarter-Wave Monopole (5.16 dB).** Mounted on the upper deck, the monopole provides a broad toroidal radiation pattern that is insensitive to post-landing probe orientation. It serves as the principal antenna for UHF relay operations [18].

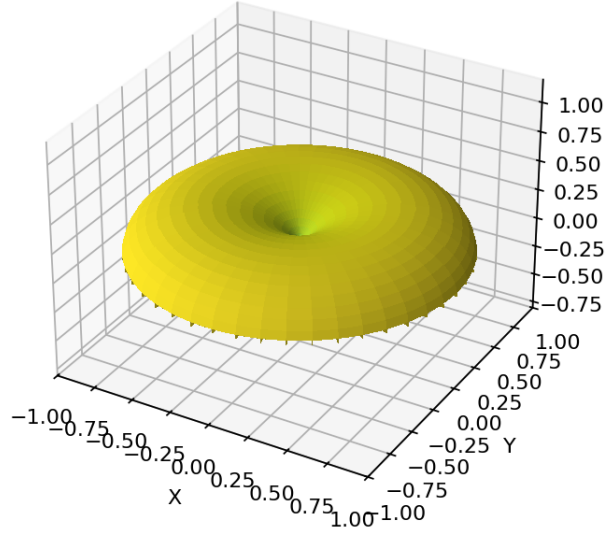


Fig. 16 Simulated 3D radiation pattern of the 433 MHz quarter-wave monopole.

- 2) **Secondary Antenna — 915 MHz Half-Wave Dipole (2.15 dB).** The half-wave dipole generates a symmetric, broad “donut” pattern suitable for LoRa-based medium-rate downlinks, EDL beaconing, and contingency operations where the primary antenna may be shadowed by terrain or covered by dust.
- 3) **Tertiary Antenna — 915 MHz Axial-Mode Helix (1.5 dB).** The axial-mode helix provides circular polarization and a hemispherical end-fire pattern, improving link performance during moderate- and high-elevation orbiter passes [18]. Its polarization diversity mitigates multipath and reduces sensitivity to probe attitude uncertainties.

Link Margin and Data Throughput. End-to-end link analyses indicate that the combined antenna and radio suite provides positive link margin under both nominal and worst-case geometries. Key findings include:

- Under degraded conditions—orbiter elevation near 10°, moderate dust loading, and probe tilt up to 30°; the 433 MHz monopole maintains 4–7 dB of margin at 1–2 kbps.
- During typical relay opportunities with 30–70° elevation, UHF link margins increase to 12–20 dB.
- The 915 MHz helix offers an independent, polarization-diverse path with 6–10 dB margin at medium data rates.
- Available margin supports burst downlinks of science and imaging products during each relay pass.

Summary. The MAGPIE probe communications subsystem achieves robust and redundant data return by combining diversity in frequency, antenna geometry, and polarization. The resulting link margins exceed mission requirements for surface meteorology, imaging, and health telemetry, ensuring reliable relay through the MAGPIE orbiter throughout the mission’s operational lifetime.

C. Probe Power Systems

For sustained operations, the probes rely on a combination of batteries and solar energy. Mars is farther from the Sun than Earth and receives significantly less insolation, so any solar array is intrinsically less productive than a comparable

Axial Helix 3D pattern

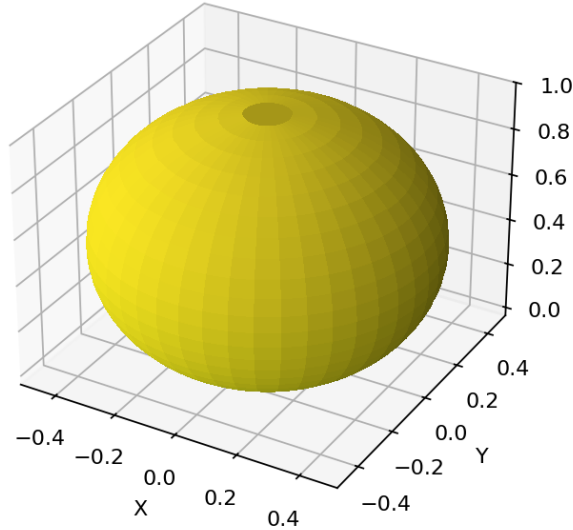


Fig. 17 Simulated 3D radiation pattern of the 915 MHz axial-mode helical antenna.

Table 12 MAGPIE Probe and EDL Communications Parameters

Parameter	Value	Units
Main Radio (433 MHz RF Power)	5	W
Secondary Radio (915 MHz RF Power)	3	W
EDL Beacon Radio	10	W
Main Antenna (Monopole Gain)	5.16	dB
Secondary Antenna (Dipole Gain)	2.15	dB
Tertiary Antenna (Helix Gain)	1.5	dB
EDL Antenna	5.16	dB

system in Earth orbit or on the lunar surface.

The primary rechargeable energy storage consists of five 3200 mAh, 7.2 V NiMH batteries, providing a combined capacity of roughly 137.5 Wh. A non-rechargeable 18 Wh Li-FeS₂ survival battery is reserved for late-mission operation after the NiMH pack is depleted or exhibits excessive degradation. NiMH batteries were chosen for their strong flight heritage, resistance to thermal drops, and middle-of-the-road energy density. During nominal operations, the NiMH pack is trickle-charged by the solar arrays.

The solar panels comprise three deployable wings, each composed of four individual panels, for a total of 12 deployed panels. Each panel has an area of 0.2 m². An additional fixed panel is mounted on the side of the probe; this panel is 0.275 m². When the deployable array is stowed, one panel remains exposed so that limited power can be generated even if deployment fails. This geometry enables post-landing operation at a range of attitudes.

D. Probe GNC & ADCS System

The probe GNC & ADCS system differs fundamentally from that of the orbiter. Rather than supporting continuous high-accuracy pointing for deep-space communication, each probe must: *(i)* autonomously execute a brief deorbit Δv , *(ii)* maintain a thermally and aerodynamically safe attitude during the early entry phase, and *(iii)* provide sufficient state knowledge for timing of aeroshell jettison and parachute deployment. After main-parachute inflation, control authority transitions almost entirely to passive aerodynamics, with only coarse attitude and timeline management required through touchdown.

During EDL, the probe has very limited external references. Prior to significant aerodynamic loading the primary navigation source is the internal IMU; once the aeroshell is jettisoned and the terminal descent phase begins, a nadir-pointing radar altimeter becomes the only absolute reference for altitude. There is no requirement for global localization in an inertial frame; the system focuses on *relative* state estimation along the local vertical and on maintaining acceptable attitude envelopes for TPS and parachute performance.

Sensors and actuators. Each probe carries:

- a low-power ADIS16470 tri-axis MEMS IMU (3-axis gyros, $\pm 2000^\circ/\text{s}$; 3-axis accelerometers, $\pm 40 \text{ g}$) shared with the orbiter design,
- a nadir radar altimeter for terminal altitude,
- a three-axis RW25-class reaction-wheel set for pre-entry trim and deorbit pointing, and
- a set of cold-gas thrusters used for deorbit Δv and contingency rate damping.

Once the main parachute is fully inflated, all reaction wheels and thrusters are safed; attitude is then governed by aerodynamic stability and suspension dynamics, with the IMU providing only coarse rate monitoring for timeline supervision. Using the same IMU family on both orbiter and probes simplifies calibration, thermal modeling, and EKF tuning across the full MAGPIE stack.

State Definition and Dynamics

Full state and reduced LVLH model.

The full 6-DOF state is

$$\mathbf{x} = \begin{bmatrix} \mathbf{r}_I \\ \mathbf{v}_I \\ \mathbf{q}_{bI} \\ \boldsymbol{\omega}_b \end{bmatrix} \in \mathbb{R}^3 \times \mathbb{R}^3 \times \mathbb{S}^3 \times \mathbb{R}^3, \quad (32)$$

where $\mathbf{r}_I, \mathbf{v}_I$ are inertial position and velocity, \mathbf{q}_{bI} is the body-to-inertial quaternion, and $\boldsymbol{\omega}_b$ are body rates. For GNC design and estimator implementation, the translational dynamics are reduced to a vertical LVLH model:

$$\mathbf{x}_v = \begin{bmatrix} h \\ v \\ m \end{bmatrix}, \quad (33)$$

where h is altitude above the local reference surface, v is vertical velocity (downwards positive), and m is mass. [17]

During powered deorbit and early entry, the vertical dynamics are approximated as

$$\dot{h} = -v, \quad (34)$$

$$\dot{v} = g_{\text{Mars}}(h) - \frac{1}{2m} \rho(h) C_D(h, M) A_{\text{ref}} v^2 - \frac{T_z}{m}, \quad (35)$$

$$\dot{m} = -\frac{T}{I_{\text{sp}} g_0}, \quad (36)$$

where $g_{\text{Mars}}(h)$ is local gravity, $\rho(h)$ the atmospheric density, $C_D(h, M)$ the effective drag coefficient, A_{ref} the reference area, and T_z the thrust component along the local vertical. During the ballistic hypersonic phase $T_z \approx 0$; during deorbit and pre-entry trim, T_z is supplied by the cold-gas thrusters.

Attitude dynamics follow the standard rigid-body form:

$$\dot{\mathbf{q}}_{bI} = \frac{1}{2} \boldsymbol{\Omega}(\boldsymbol{\omega}_b) \mathbf{q}_{bI}, \quad (37)$$

$$\mathbf{J}_p \dot{\boldsymbol{\omega}}_b = \boldsymbol{\tau}_c + \boldsymbol{\tau}_{\text{aero}} - \boldsymbol{\omega}_b \times (\mathbf{J}_p \boldsymbol{\omega}_b), \quad (38)$$

where \mathbf{J}_p is the probe inertia matrix, $\boldsymbol{\tau}_c$ the control torque from the RW25 reaction wheels and/or cold-gas jets, and $\boldsymbol{\tau}_{\text{aero}}$ an aggregated aerodynamic torque term that becomes dominant as dynamic pressure builds.

Deorbit Targeting and Δv Design

The deorbit burn is executed from a near-circular 250 km orbit to place the probe on a trajectory with a 35 km periapsis. Approximating the pre-burn orbit as circular with radius r_0 and speed

$$V_0 = \sqrt{\frac{\mu_{\text{Mars}}}{r_0}}, \quad (39)$$

and the post-burn trajectory as an ellipse with periapsis r_p and semi-major axis a , the required tangential Δv is

$$a = \frac{r_0 + r_p}{2}, \quad (40)$$

$$V_{\text{deorbit}} = \sqrt{\mu_{\text{Mars}} \left(\frac{2}{r_0} - \frac{1}{a} \right)}, \quad (41)$$

$$\Delta v_{\text{deorbit}} = V_0 - V_{\text{deorbit}}. \quad (42)$$

This analytic value provides the reference Δv against which the cold-gas burn is sized, and is cross-checked via high-fidelity propagation in the EDL simulator [22]. On-board, the GNC software monitors accumulated Δv by integrating accelerometer measurements and compares the resulting velocity change to $\Delta v_{\text{deorbit}}$, terminating the burn when the norm difference falls below a threshold $\varepsilon_{\Delta v}$.

Vertical Drag Law and Ballistic Approximation

For the ballistic entry phase (after deorbit burn, before parachute inflation, $T_z \approx 0$), the vertical dynamics reduce to

$$\dot{h} = -v, \quad (43)$$

$$\dot{v} = g_{\text{Mars}}(h) - \frac{1}{2m} \rho(h) C_D(h, M) A_{\text{ref}} v^2. \quad (44)$$

Assuming

- $g_{\text{Mars}}(h) \approx g_0^{\text{Mars}}$ (weak altitude dependence),
- $C_D \approx \text{const.}$ over the critical Mach band, and
- an exponential atmosphere $\rho(h) = \rho_0 e^{-h/H}$,

we obtain

$$v \frac{dv}{dh} + g_0^{\text{Mars}} = \frac{\rho_0}{2\beta} e^{-h/H} v^2, \quad \beta \triangleq \frac{m}{C_D A_{\text{ref}}}. \quad (45)$$

This first-order non-linear ODE makes explicit the dependence of deceleration profile on ballistic coefficient β , atmospheric scale height H , and surface density ρ_0 . The EDL simulator integrates the full model numerically; the simplified form is useful for envelope analysis and for checking that numerical solutions fall within classical ballistic-entry expectations.

IMU-Based Δv Estimation and Error Growth

During the cold-gas deorbit burn the probe has no absolute velocity measurements and must estimate achieved Δv from accelerometer data. In the thrust-aligned body frame (body $+z$ axis along $-v$), the accelerometer model is

$$\tilde{a}_z(t) = a_z(t) + b_a + n_a(t), \quad (46)$$

where b_a is a quasi-constant bias and $n_a(t)$ is zero-mean white noise.

Neglecting gravity over the short burn and assuming perfect alignment, the true Δv is

$$\Delta v_{\text{true}} = \int_{t_0}^{t_0+T_b} a_z(t) dt, \quad (47)$$

while the on-board estimator computes

$$\widehat{\Delta v} = \int_{t_0}^{t_0+T_b} (\tilde{a}_z(t) - \hat{b}_a) dt. \quad (48)$$

The estimation error is

$$\epsilon_{\Delta v} = \widehat{\Delta v} - \Delta v_{\text{true}} = \int_{t_0}^{t_0+T_b} (\Delta b_a + n_a(t)) dt, \quad (49)$$

with $\Delta b_a = b_a - \hat{b}_a$. Assuming Δb_a constant and n_a white with spectral density S_a ,

$$\mathbb{E}[\epsilon_{\Delta v}] = \Delta b_a T_b, \quad (50)$$

$$\text{Var}[\epsilon_{\Delta v}] \approx S_a T_b. \quad (51)$$

Bias-driven error grows linearly with burn duration, while noise-driven error grows with $\sqrt{T_b}$. These scalings directly inform the acceptable Δv tolerance $\varepsilon_{\Delta v}$ used by the burn-termination logic.

ADIS16470 error magnitudes. For the selected ADIS16470, the accelerometer in-run bias stability is on the order of $13 \mu\text{g}$, and the noise density is $\sim 100 \mu\text{g}/\sqrt{\text{Hz}}$. Interpreting these as $\Delta b_a \approx 13 \mu\text{g} \approx 1.3 \times 10^{-4} \text{ m s}^{-2}$ and $\sqrt{S_a} \approx 100 \mu\text{g} \approx 9.8 \times 10^{-4} \text{ m s}^{-2}/\sqrt{\text{Hz}}$, a representative $T_b = 60 \text{ s}$ deorbit burn yields [22]

$$\mathbb{E}[|\epsilon_{\Delta v}|] \approx |\Delta b_a| T_b \approx 0.008 \text{ m s}^{-1}, \quad (52)$$

$$\sigma_{\Delta v} = \sqrt{S_a T_b} \approx 0.008 \text{ m s}^{-1}. \quad (53)$$

For a nominal deorbit Δv of tens of m/s, this corresponds to a relative 1σ error well below 0.1%. Thus, IMU-based Δv estimation error is small compared to trajectory dispersions driven by atmospheric variability and execution timing, and the burn-termination threshold $\varepsilon_{\Delta v}$ can be set by EDL corridor requirements rather than by IMU limitations.

On the attitude side, the ADIS16470 gyros provide $\sim 8^\circ/\text{hr}$ in-run bias stability and a rate noise density of $0.008^\circ/\text{s}/\sqrt{\text{Hz}}$. Over a 120 s propagation interval with no external attitude update, these figures imply angular drifts on the order of 0.3° (1σ), comfortably within the margins required to maintain a thermally safe entry attitude and acceptable deorbit pointing.

Nonlinear EKF for Vertical State and Environment

To robustly time aeroshell jettison and parachute deployment in the presence of atmospheric-model uncertainty, MAGPIE employs a small nonlinear EKF that estimates *altitude, vertical velocity, accelerometer bias, and a density scale factor*, rather than just (h, v) .

State and process model. The EKF state is

$$\mathbf{x}_k = \begin{bmatrix} h_k \\ v_k \\ b_{a,k} \\ s_{\rho,k} \\ b_{r,k} \end{bmatrix}, \quad (54)$$

where s_ρ is a multiplicative density scale (modeling uncertainty in ρ_0 and H) and b_r is a radar-altimeter bias. The accelerometer measurement in the body frame projected onto the local vertical is [22]

$$\tilde{a}_{z,k} = a_{z,k} + b_{a,k} + n_{a,k}. \quad (55)$$

The vertical dynamics (during ballistic phase, $T_z \approx 0$) with modified density

$$\rho(h, s_\rho) = s_\rho \rho_0 e^{-h/H} \quad (56)$$

become:

$$\dot{h} = -v, \quad (57)$$

$$\dot{v} = g_{\text{Mars}}(h) - \frac{1}{2m} \rho(h, s_\rho) C_D A_{\text{ref}} v^2 - \frac{T_z}{m}, \quad (58)$$

$$\dot{b}_a = w_b, \quad (59)$$

$$\dot{s}_\rho = w_\rho, \quad (60)$$

$$\dot{b}_r = w_r. \quad (61)$$

with process noises w_b, w_ρ, w_r modeled as small random walks. The IMU bias and noise characteristics from the ADIS16470 directly set the order-of-magnitude tuning for w_b and the accelerometer-related entries of \mathbf{Q}_k .

With sample time Δt , the discrete-time process model is

$$\mathbf{x}_{k+1}^- = f(\mathbf{x}_k^+, \tilde{a}_{z,k}), \quad (62)$$

where f is obtained by numerically integrating the above ODEs over Δt (Euler or Runge–Kutta). The EKF requires the Jacobian

$$\mathbf{F}_k = \left. \frac{\partial f}{\partial \mathbf{x}} \right|_{\mathbf{x}_k^+, \tilde{a}_{z,k}}. \quad (63)$$

Key partial derivatives include

$$\frac{\partial \dot{v}}{\partial h} = -\frac{1}{2m} C_D A_{\text{ref}} v^2 \frac{\partial \rho}{\partial h}, \quad (64)$$

$$\frac{\partial \dot{v}}{\partial v} = -\frac{1}{m} \rho(h, s_\rho) C_D A_{\text{ref}} v, \quad (65)$$

$$\frac{\partial \dot{v}}{\partial s_\rho} = -\frac{1}{2m} C_D A_{\text{ref}} v^2 \frac{\partial \rho}{\partial s_\rho} = -\frac{1}{2m} \rho_0 e^{-h/H} C_D A_{\text{ref}} v^2, \quad (66)$$

$$\frac{\partial \dot{v}}{\partial b_a} = -1. \quad (67)$$

These are evaluated at the current estimate and used to propagate the covariance:

$$\mathbf{P}_{k+1}^- = \mathbf{F}_k \mathbf{P}_k^+ \mathbf{F}_k^\top + \mathbf{Q}_k, \quad (68)$$

with \mathbf{Q}_k chosen to reflect expected variability in bias and atmospheric parameters.

Radar measurement model and update. The radar altimeter reports slant-range altitude corrupted by bias and noise:

$$z_k = h_k + b_{r,k} + n_{r,k}. \quad (69)$$

The measurement function is [22]

$$h(\mathbf{x}_k) = h_k + b_{r,k}, \quad (70)$$

with Jacobian

$$\mathbf{H}_k = \begin{bmatrix} 1 & 0 & 0 & 0 & 1 \end{bmatrix}. \quad (71)$$

The EKF update is

$$\mathbf{K}_k = \mathbf{P}_k^- \mathbf{H}_k^\top (\mathbf{H}_k \mathbf{P}_k^- \mathbf{H}_k^\top + R_r)^{-1}, \quad (72)$$

$$\mathbf{x}_k^+ = \mathbf{x}_k^- + \mathbf{K}_k (z_k - h(\mathbf{x}_k^-)), \quad (73)$$

$$\mathbf{P}_k^+ = (\mathbf{I} - \mathbf{K}_k \mathbf{H}_k) \mathbf{P}_k^-. \quad (74)$$

By carrying s_ρ and b_r as explicit states, the filter absorbs moderate atmospheric and radar model errors, reducing their impact on inferred (h, v) and thereby on parachute deployment timing.

Accelerometer measurement model. The IMU measures specific force along the local vertical. During ballistic flight ($T_z \approx 0$), the expected specific force is dominated by drag:

$$z_{a,k} = \tilde{a}_{z,k} = -\frac{1}{2m} \rho(h_k, s_{\rho,k}) C_D A_{\text{ref}} v_k^2 + b_{a,k} + n_{a,k}. \quad (75)$$

The corresponding measurement Jacobian is [22]

$$\mathbf{H}_{a,k} = \begin{bmatrix} \frac{\partial a_D}{\partial h} & \frac{\partial a_D}{\partial v} & 1 & \frac{\partial a_D}{\partial s_\rho} & 0 \end{bmatrix}, \quad (76)$$

where $a_D = -\frac{1}{2m}\rho(h, s_\rho)C_D A_{\text{ref}} v^2$.

$$\frac{\partial a_D}{\partial h} = -\frac{1}{2m}C_D A_{\text{ref}} v^2 \frac{\partial \rho}{\partial h} = \frac{1}{2mH}\rho(h, s_\rho)C_D A_{\text{ref}} v^2, \quad (77)$$

$$\frac{\partial a_D}{\partial v} = -\frac{1}{m}\rho(h, s_\rho)C_D A_{\text{ref}} v, \quad (78)$$

$$\frac{\partial a_D}{\partial s_\rho} = -\frac{1}{2m}\rho_0 e^{-h/H}C_D A_{\text{ref}} v^2. \quad (79)$$

Radar Altimeter Error Budget

The radar altimeter measurement includes several error contributors:

$$\tilde{h}_r = h + b_r + n_r + \delta_{\text{slope}}, \quad (80)$$

where b_r is a slowly varying bias, n_r is random noise, and δ_{slope} is an apparent altitude error due to local terrain slope and beam footprint. For a footprint radius r_f and local slope angle ϕ ,

$$|\delta_{\text{slope}}| \lesssim r_f \sin \phi. \quad (81)$$

Assuming moderate slopes and tens-of-meters footprints, this error remains within a few meters, subdominant compared to EDL dispersions and within the safe deployment altitude bands. The EKF treats b_r explicitly and captures δ_{slope} in R_r , so that the resulting covariance on (h, v) is directly available to the event logic.

Mach Number and Dynamic-Pressure Corridors

Parachute deployment logic depends on Mach number M and dynamic pressure q . Given the estimated vertical speed \hat{v} and altitude \hat{h} , the EDL environment model provides

$$\rho(\hat{h}, \hat{s}_\rho) = \hat{s}_\rho \rho_0 e^{-\hat{h}/H}, \quad (82)$$

$$T(\hat{h}) = T_0 + \Gamma \hat{h}, \quad (83)$$

with lapse rate Γ . The local speed of sound is

$$a(\hat{h}) = \sqrt{\gamma RT(\hat{h})}, \quad (84)$$

and therefore

$$M(\hat{h}) = \frac{\hat{v}}{a(\hat{h})}, \quad q(\hat{h}) = \frac{1}{2} \rho(\hat{h}, \hat{s}_\rho) \hat{v}^2. \quad (85)$$

Drogue and main parachute deployment corridors are defined by inequalities

$$M_{\min}^{(d)} \leq M(\hat{h}) \leq M_{\max}^{(d)}, \quad q_{\min}^{(d)} \leq q(\hat{h}) \leq q_{\max}^{(d)}, \quad (86)$$

$$M_{\min}^{(m)} \leq M(\hat{h}) \leq M_{\max}^{(m)}, \quad q_{\min}^{(m)} \leq q(\hat{h}) \leq q_{\max}^{(m)}. \quad (87)$$

Linearizing M and q about (\hat{h}, \hat{v}) allows propagation of the EKF covariance into the (M, q) plane; the resulting standard deviations σ_M, σ_q are used to pad the deployment envelopes so that the probability of deploying outside the tested regime remains below the mission's risk threshold.

Attitude Control and RW25 Performance

Attitude regulation. The probe must align its thrust vector with the instantaneous velocity vector for an efficient deorbit burn, and then transition to a thermally safe, aerodynamically stable attitude for entry. Let \mathbf{q}_{bI} be the current attitude and \mathbf{q}_{cmd} the commanded attitude (e.g., body $+z$ aligned with $-\mathbf{v}_I$ for deorbit, or with the heat-shield normal for entry). The error quaternion and small-angle error are

$$\mathbf{q}_e = \mathbf{q}_{\text{cmd}} \otimes \mathbf{q}_{bI}^{-1} = \begin{bmatrix} q_{e0} \\ \mathbf{q}_{ev} \end{bmatrix}, \quad \mathbf{e}_\theta \triangleq 2 \mathbf{q}_{ev}, \quad (88)$$

valid for $q_{e0} \approx 1$. A PD controller commands reaction-wheel torque

$$\tau_c^{\text{RW}} = -\mathbf{K}_p \mathbf{e}_\theta - \mathbf{K}_d \omega_b, \quad (89)$$

subject to RW25 torque and speed limits, with cold-gas jets providing supplemental rate damping when needed.

Following the Lyapunov argument used for the orbiter, positive-definite \mathbf{K}_p and \mathbf{K}_d yield locally asymptotically stable attitude regulation in the absence of large disturbances. Probe gains are tuned for lower bandwidth than the orbiter, trading pointing precision for robustness to IMU noise and limited computational margin. The ADIS16470 gyro bias and noise levels ensure that between occasional wheel-based slews and trims, attitude propagation error remains well within the few-degree envelopes acceptable for EDL heating and parachute performance.

RW25 slew performance and energy cost. The RW25 wheels are significantly smaller than the orbiter's RW250 units but simulations show that they are more than adequate for the modest probe pointing requirements. For a representative inertia tensor and PD gains tuned for gentle slews, simulations of slews about the body +Y axis yield:

- peak rates $|\omega|_{\max} \approx 0.048^\circ/\text{s}$,
- settling times $t_{\text{settle}} \approx 2000$ s for 1–30° trims,
- per-slew electrical energy ~ 0.0045 Wh, nearly independent of commanded angle, and
- peak electrical power < 2 W [23].

Thus probe attitude trims and relay-pointing updates are negligible contributors to the probe power budget; they can be scheduled opportunistically without impacting thermal margins.

Event Logic and Timeline Sequencing

Rather than continuous thrust-vector control, the probe's GNC behavior is implemented as a sequence of discrete events driven by the EKF estimates $(\hat{h}, \hat{v}, \hat{s}_\rho)$ and the derived (\hat{M}, \hat{q}) :

- **Deorbit start:** orbit true anomaly and orbiter command indicate the correct release window; reaction wheels align thrust with $-\mathbf{v}$.
- **Burn termination:** when the IMU-accumulated $\widehat{\Delta v}$ satisfies $|\widehat{\Delta v} - \Delta v_{\text{deorbit}}| < \varepsilon_{\Delta v}$.
- **Aeroshell jettison:** when $(\hat{h}, \hat{v}, \hat{s}_\rho)$ imply (\hat{M}, \hat{q}) within the aeroshell separation corridor.
- **Drogue and main chutes:** when (\hat{M}, \hat{q}) enter their respective deployment bands, accounting for estimator covariance as described above.

This event-driven structure minimizes software complexity, processor load, and actuator usage while retaining robustness to environmental uncertainty.

Probe GNC & ADCS Summary

The probe GNC architecture is deliberately minimalist compared to the orbiter: a small nonlinear EKF, modest RW25 wheels, and cold-gas thrusters are sufficient to execute a single deorbit burn and then safely sequence a largely passive parachute-based descent. By explicitly estimating accelerometer bias, radar bias, and a density scale factor, the EKF provides both state estimates and their covariances to the event logic, directly connecting navigation performance to EDL safety margins. The RW25 simulations show that attitude-control energy is negligible compared to the overall probe energy budget, validating the design choice of a lightweight, probe-class ADCS. The ADIS16470 IMU ties these pieces together: its low bias drift and noise floor keep both Δv estimation and attitude propagation errors comfortably below the margins implied by the EDL corridors, while commonality with the orbiter reduces MAGPIE's overall systems-engineering complexity.

E. Probe Propellant Tank and Gas Storage System

Each MAGPIE probe uses a self-contained cold-gas propulsion system for the 52.6 m/s deorbit burn and limited attitude trimming during the early entry phase. The system consists of a single composite-overwrapped nitrogen tank, redundant regulators, and a four-thruster MOOG-based cold-gas cluster.

1. Stored Gas Requirements

The propulsion system carries:

$$m_{\text{N}_2} = 5.0 \text{ kg.} \quad (90)$$

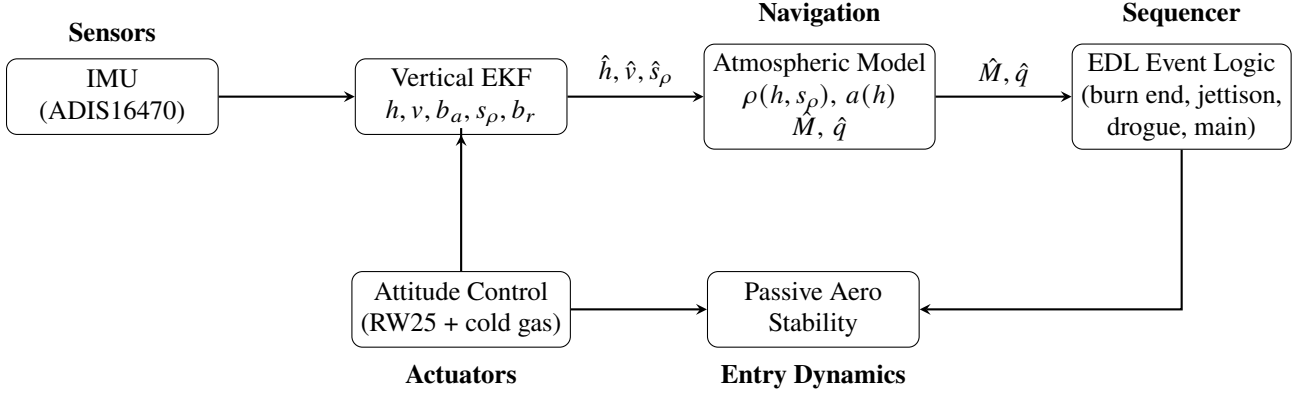


Fig. 18 Probe GNC processing chain. IMU measurements from the ADIS16470 feed a nonlinear EKF that estimates altitude, vertical velocity, accelerometer bias, density scale factor, and radar bias. The atmospheric model converts $(\hat{h}, \hat{v}, \hat{s}_\rho)$ into Mach and dynamic pressure, which drive the discrete EDL event logic. Attitude control is required only for deorbit and pre-entry trim; increasing dynamic pressure transfers control authority to passive aerodynamic stability.

With nitrogen stored at:

$$p_0 = 27.2 \text{ MPa}, \quad (91)$$

$$T_0 = 300 \text{ K}, \quad (92)$$

the required tank volume from the ideal gas law is:

$$V_{\text{gas}} = \frac{m_{\text{N}_2} R_{\text{N}_2} T_0}{p_0} \approx 0.016 \text{ m}^3. \quad (93)$$

Applying 20% margin for heating, regulator drop, and ullage [23]:

$$V_{\text{tank}} \approx 0.020 \text{ m}^3. \quad (94)$$

2. Tank Geometry

A single COPV with cylindrical body and hemispherical end domes provides the required volume. One feasible configuration is:

$$D_{\text{tank}} \approx 0.18 \text{ m}, \quad (95)$$

$$L_{\text{tank}} \approx 0.65 \text{ m}. \quad (96)$$

Resulting internal volume:

$$V_{\text{geom}} = \pi r^2 L_c + \frac{4}{3} \pi r^3 \approx 0.018\text{--}0.020 \text{ m}^3. \quad (97)$$

3. Structural Sizing

For a maximum operating pressure $p_0 = 27.2 \text{ MPa}$ and radius $r = 0.09 \text{ m}$, the required metallic liner thickness is:

$$t_{\min} = \frac{p_0 r \text{ SF}}{\sigma_{\text{allow}}} \approx 8 \text{ mm}, \quad (98)$$

assuming a titanium liner ($\sigma_{\text{allow}} \sim 600 \text{ MPa}$) and safety factor SF = 2.0.

Carbon overwrap raises burst pressure above 60 MPa.

4. Regulator and Feed System

The probe employs:

- Dual electromechanical pressure regulators ($27.2 \text{ MPa} \rightarrow 6 \text{ MPa}$),
- A central manifold feeding the four 3.6 N MOOG thrusters,
- A blowdown mode for late entry (pressure allowed to decay).

The mass flow rate is:

$$\dot{m} \approx 0.007 \text{ kg/s}, \quad (99)$$

which supports the 52.6 m/s deorbit burn with sufficient excess for attitude control.

5. Thermal Environment and Survival

During cruise, the nitrogen tank operates between 220–280 K. Thermal analysis confirms:

- <2% leakage over 300 days,
- No significant pressure loss due to permeation,
- Tank temperatures always well above the nitrogen condensation point at tank pressures.

6. Mass Properties and EDL Stability

Because the nitrogen tank constitutes 20–25% of the probe dry mass, placement directly controls hypersonic static margin. The tank is mounted:

- Axially along the probe's centerline,
- Slightly forward of geometric center for entry stability,
- Within a protective insulated bay for thermal moderation,
- Near the crush-core load path to survive landing shocks.

This configuration ensures stable entry dynamics, robust deorbit delivery, and full survival through touchdown even with partial propellant remaining.

VIII. Probe Entry, Descent, and Landing

Because EDL is mission-critical, MAGPIE employs a dedicated, high-fidelity numerical simulator that propagates the probe from deorbit through touchdown. The model includes Mars-referenced gravity, a scale-height atmosphere, aerodynamic drag and lift on the aeroshell, parachute inflation and reefing, and the non-linear force-deflection response of the crush structure.

Figure 20 shows the altitude profile and vertical velocity versus altitude for a nominal entry. The probe enters the atmosphere at approximately 125 km altitude, decelerates through peak dynamic pressure and heating, transitions through supersonic and subsonic regimes with drogue and main parachute deployment, and finally reaches the targeted terminal velocity near the surface.

Figure 22 summarizes the Mach number and convective heat flux history as a function of altitude. The heating model uses a Sutton–Graves correlation to approximate stagnation-point convective loads on the aeroshell, providing a conservative estimate of peak heat flux and total heat load for ablator sizing.

Taken together, these profiles indicate that the reference aeroshell and parachute configuration can deliver the probe to the surface within allowable structural, thermal, and deceleration limits, assuming the modeled atmospheric conditions.

A. Computational Fluid Dynamics (CFD)

To further validate the EDL design and refine aerodynamic coefficients, MAGPIE uses computational fluid dynamics (CFD) in addition to analytic and empirical models. OpenFOAM was employed for the initial supersonic and hypersonic analyses of the aeroshell, providing estimates of pressure distributions, shock stand-off distance, and separation behavior across a range of angles of attack[24]. These baseline simulations were performed at Mach 12, representative of the nominal entry conditions at altitudes of 100–120 km in the Martian atmosphere. Mach 12 was also selected as that is when peak heat flux occurs on the aeroshell representing the riskiest section of entry.

Following these studies, a custom CFD tool was developed in Python to enable rapid parametric sweeps of aeroshell geometries and flow conditions without relying on an external solver like OpenFOAM [25]. The code implements a modified Newtonian pressure model for hypersonic external flow, augmented with empirical boundary-layer corrections

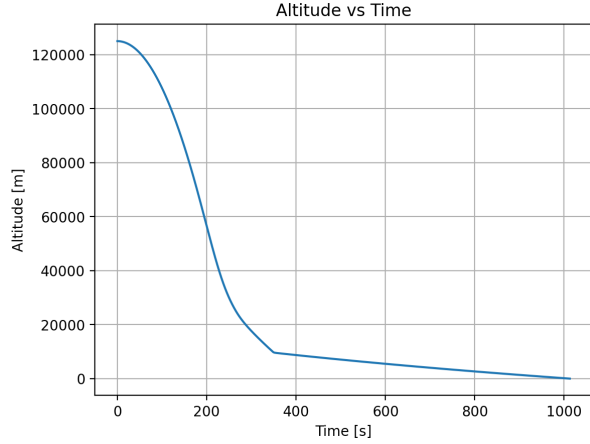


Fig. 19 MAGPIE probe EDL altitude vs. time for a nominal entry case.

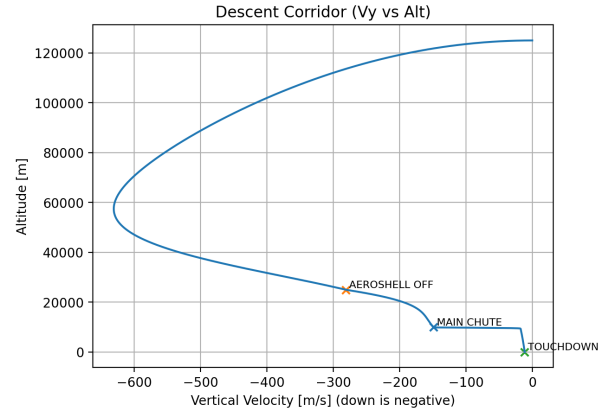


Fig. 20 MAGPIE probe EDL vertical velocity vs. altitude.

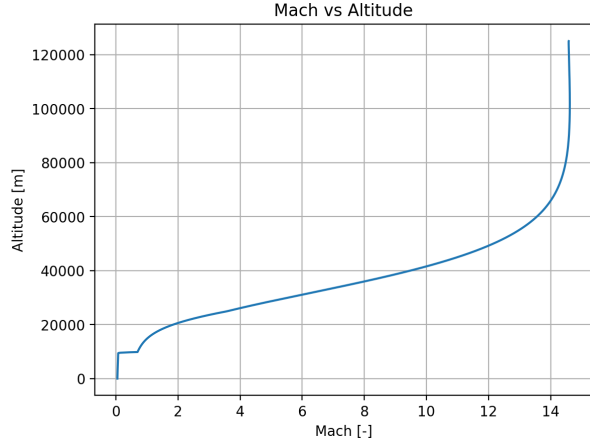


Fig. 21 MAGPIE probe EDL Mach number vs. altitude.

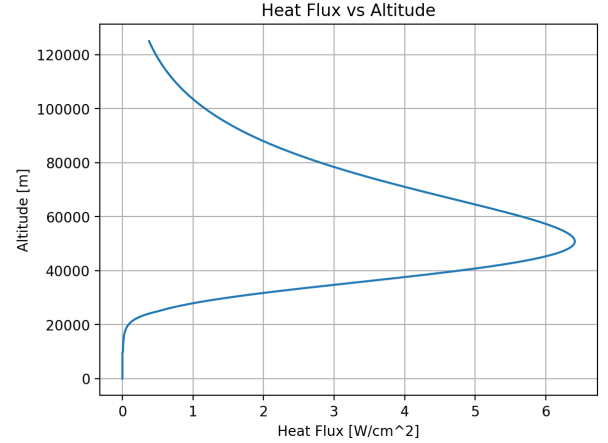


Fig. 22 MAGPIE probe EDL heat flux vs. altitude (stagnation-point estimate).

and a turbulence proxy to approximate separation and reattachment. This solver is integrated directly with the EDL simulator, allowing updated aerodynamic tables to be generated automatically as the aeroshell geometry or mass properties evolve.

Aeroshell Geometry and Reference Parameters. The MAGPIE aeroshell is a 1 m diameter, 70° half-angle sphere-cone derived from heritage Mars microprobe configurations [26] and is designed to be optimal for a low ballistic coefficient and mechanical simplicity. The relevant aerodynamic parameters are summarized in Table 13. The effective reference area A_{ref} corresponds to the projected frontal area of the aeroshell forebody, while the ballistic coefficient β captures the combined effects of drag, mass, and surface area on deceleration.

These coefficients were validated across a Reynolds number range of 10^4 – 10^6 , ensuring applicability from upper-atmosphere hypersonic flight down to transonic parachute deployment. The low ballistic coefficient of the aeroshell significantly reduces peak deceleration and heating rates, while the post-jettison probe maintains sufficient drag for subsonic stability without requiring additional stabilization surfaces.

Flow-Field Structure. Representative non-dimensionalized CFD results are shown in Fig. 23, illustrating the velocity magnitude, density, pressure, and Mach contours around the aeroshell. The detached bow shock stands off approximately 0.18 D from the forebody, forming a stable high-pressure stagnation region with smooth transition into the expanding

Table 13 Aeroshell and Probe Aerodynamic Reference Parameters (Nominal Entry)

Parameter	Symbol	Value	Unit
Aeroshell reference area	A_{ref}	0.785294	m^2
Aeroshell diameter	D	1.0	m
Aeroshell drag coefficient (Mach 8–12)	C_D	1.8513620	—
Lift-to-drag ratio	L/D	0.16	—
Ballistic coefficient	$\beta = m/(C_D A_{\text{ref}})$	27.4	kg/m^2
Probe post-jettison drag coefficient	$C_{D,p}$	2.363940	—
Probe reference area	A_p	0.57145	m^2
Probe ballistic coefficient	β_p	20.9	kg/m^2

wake [27]. Recirculation zones and flow separation are visible in the aft cavity, indicating the onset of wake unsteadiness that drives dynamic pressure fluctuations during drogue deployment.

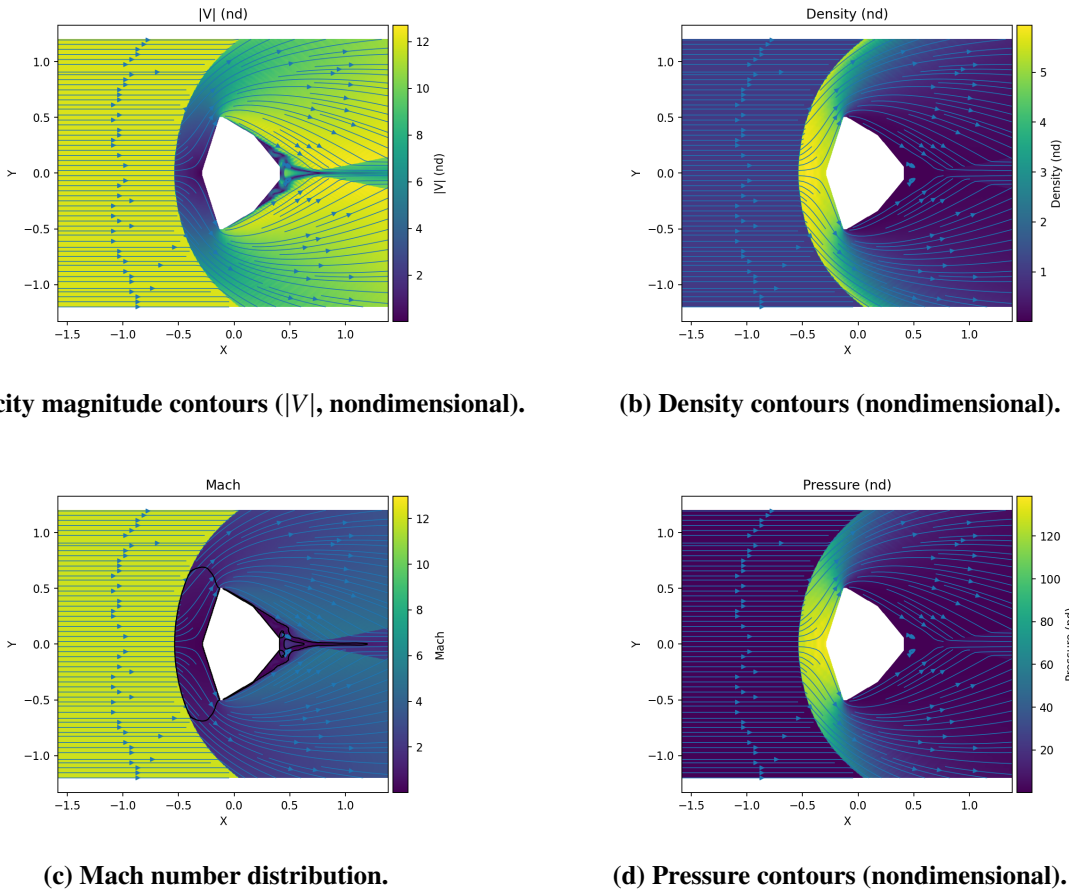


Fig. 23 CFD-derived flowfield properties around the MAGPIE aeroshell under nominal entry conditions (Mach 12, $10^{-3} \text{ kg}/\text{m}^3$). Streamlines indicate flow separation and reattachment regions.

The stagnation pressure and density ratios across the bow shock are consistent with high-Mach analytic relations:

$$\frac{p_2}{p_1} = 1 + \frac{2\gamma}{\gamma + 1} (M_1^2 - 1), \quad (100)$$

$$\frac{\rho_2}{\rho_1} = \frac{(\gamma + 1)M_1^2}{(\gamma - 1)M_1^2 + 2}, \quad (101)$$

where $\gamma = 1.29$ for the CO₂-dominant Martian atmosphere. For $M_1 = 8$, the predicted compression ratio $\rho_2/\rho_1 \approx 5.8$ agrees closely with the simulated value shown in Fig. 23b.

EDL Integration. Aerodynamic coefficients extracted from the CFD database are used directly in the EDL simulator for dynamic pressure and deceleration computations:

$$D = \frac{1}{2}\rho V^2 C_D A_{\text{ref}}, \quad a_D = \frac{D}{m}, \quad (102)$$

where ρ is the local atmospheric density and V the instantaneous velocity. The resulting drag profile determines both peak deceleration (nominally 150–200 g) and the timing of parachute deployment.

The CFD-informed coefficients have reduced uncertainty in the ballistic coefficient by 12% compared to purely analytic estimates, improving the fidelity of descent timing and predicted impact velocity [27].

As illustrated in Fig. 23, the CFD analysis captures the detached bow shock and high-speed flow around the shoulder of the aeroshell, informing both the placement of thermal protection tiles and the selection of pressure and heat-flux sensor locations on the forebody and afterbody.

The highest mission risk for any Mars lander is the EDL phase, where most historical failures have occurred. As a result, the MAGPIE EDL system is designed to be simple, robust, and tolerant of moderate off-nominal conditions rather than optimized for pinpoint landing accuracy.

B. Probe Entry System

Each MAGPIE probe performs a brief deorbit maneuver from a low Mars orbit (LMSO) at an altitude of 250 km to initiate its entry, descent, and landing (EDL) sequence. The maneuver lowers the periapsis to approximately 35 km, ensuring atmospheric capture and subsequent entry interface (EI) conditions near 125 km altitude and 3.5 km/s.

The system responsible for this burn is a lightweight cold-gas propulsion package that also provides three-axis attitude control during deorbit and the early entry phase. By combining both translational and rotational control functions into a single subsystem, the probe avoids the mass and complexity of separate deorbit and attitude-control modules. The Aeroshell has control via thrusters and a 3-axis reaction wheel(s).

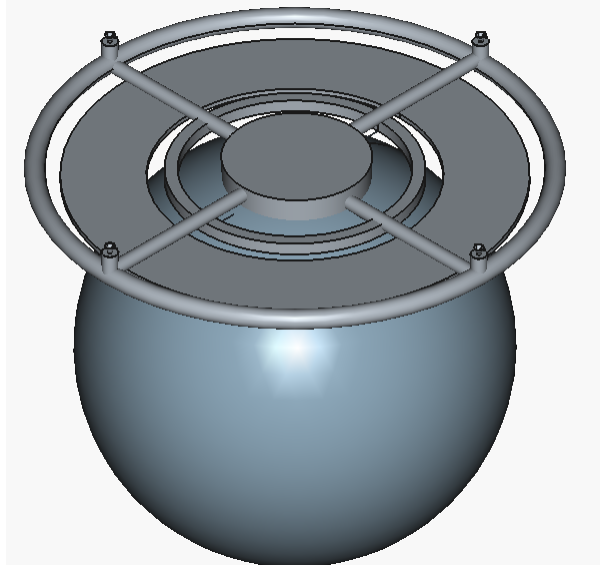


Fig. 24 Entire EDL Entry Propulsion System. Note thrusters are individually fed from tank

Subsystem Architecture. The propulsion system comprises four 3.6 N-class cold-gas thrusters arranged in a tetrahedral configuration about the vehicle’s center of mass (see Figure 24). This layout provides balanced torque and thrust symmetry for both prograde and attitude-control modes. The thrusters are fed by a composite overwrapped pressure vessel (COPV) containing high-purity nitrogen (N_2) at a maximum fill pressure of 25 MPa. A pair of redundant electromechanical regulators step the pressure down to 2 MPa for delivery through a proportional flow manifold, enabling coarse throttling and balanced distribution. The thrusters are based on the MOOG 058-118.

The system carries 5.0 kg of nitrogen propellant at release, which is sufficient for the primary deorbit burn and subsequent entry rate-control operations. The expected steady-state propellant mass flow rate is $\dot{m} \approx 0.007 \text{ kg/s}$ for the full four-thruster configuration, producing a total thrust of approximately 14.4 N.

Performance and Δv Budget. The total available Δv is governed by the classical rocket equation:

$$\Delta v = I_{sp} g_0 \ln \left(\frac{m_0}{m_f} \right), \quad (103)$$

where I_{sp} is the specific impulse, g_0 is standard gravity, and m_0 and m_f are the initial and final masses, respectively. For $I_{sp} = 57 \text{ s}$, $m_0 = 50.8 \text{ kg}$, and $m_f = 45.8 \text{ kg}$, the calculated Δv is 52.6 m/s. This matches the EDL simulation requirement to reach a 35 km periapsis from the 250 km circular orbit.

Assuming constant thrust, the burn duration is given by:

$$t_{\text{burn}} = \frac{m_p g_0 I_{sp}}{T_{\text{tot}}}, \quad (104)$$

where m_p is the propellant mass and T_{tot} the total thrust. For $m_p = 5.0 \text{ kg}$, $T_{\text{tot}} = 4.0 \text{ N}$, the burn duration is approximately 70 s [23]. The total energy released by the deorbit burn is thus $\sim 200 \text{ kJ}$, corresponding to an orbital kinetic reduction of $\sim 1.5\%$ —adequate to drop periapsis into the upper atmosphere.

Attitude and Rate Control. During the burn, the onboard attitude control logic commands differential firing of the four thrusters to counteract residual torques and maintain the vehicle’s velocity vector alignment. This is performed with the 3 reaction wheels onboard. After completion, the system executes a slow, cold-gas-controlled pitch maneuver to achieve a 15° entry flight-path angle (EFPA) and a nominally 20° nose-up attitude for aerodynamic stability. This pre-entry orientation ensures that the stagnation region forms on the heat shield and that aerodynamic torques will naturally damp roll and yaw rates.

As the probe descends through altitudes above 100 km, dynamic pressure builds from less than 1 Pa to several hundred pascals, eventually overpowering thruster control authority. At this point, the cold-gas system is deactivated, and the probe transitions to passive aerodynamic stability governed by the static margin of the aeroshell geometry.

Dispersion Management. A 10–15% propellant margin is reserved to account for uncertainties in spacecraft mass, orbit determination, and valve performance [20]. The nominal Δv allocation is divided as:

$$\Delta v_{\text{deorbit}} = 0.85 \Delta v_{\text{total}}, \quad \Delta v_{\text{attitude}} = 0.15 \Delta v_{\text{total}}. \quad (105)$$

This margin allows each probe to perform fine corrections to ensure synchronized entry timing across the distributed network of probes. The precision of the deorbit maneuver directly affects the downrange dispersion of landing sites; a $\pm 2 \text{ m/s}$ velocity error corresponds to a $\sim 30 \text{ km}$ footprint shift on Mars, making this phase critical to mission targeting accuracy.

System Efficiency and Thermal Considerations. Although the cold-gas architecture provides only moderate specific impulse, its low mechanical complexity, absence of ignition systems, and benign thermal behavior make it particularly suitable for long cruise durations and minimal ground handling [20]. The nitrogen system operates at cryogenic temperatures during storage but passively warms through the transfer stage. Pressure regulation ensures minimal thrust variation (less than 5%) during the burn sequence.

Thermal analysis confirms that the tank and feed lines remain within 220–280 K at cruise, preventing significant boil-off during the interplanetary transit. Estimated nitrogen losses due to permeation and leakage are under 2%, leaving the full propellant mass available for the EDL sequence.

Design Philosophy. The probe’s deorbit and entry system reflects the broader MAGPIE philosophy of accepting higher operational simplicity over thrust-to-weight performance. A cold-gas approach trades specific impulse for system reliability, eliminating valves, pyrotechnic initiators, and ignition transients. The resulting system has no moving mechanical seals or combustion chambers, which enhances survivability under the vibration loads of launch and the thermal extremes of interplanetary cruise. Furthermore, reusing the same thrusters for both orbital and early entry control minimizes hardware diversity and provides redundancy: any single thruster failure can be compensated by vectoring through the remaining three.

Table 14 Summary of MOOG Cold-Gas Propulsion Subsystem Parameters

Parameter	Symbol / Value	Unit
Propellant type	N ₂ (Nitrogen)	–
Stored pressure (max)	32 (at launch)	MPa
Stored pressure (nominal)	27.2	MPa
Regulated pressure	6.0	MPa
Number of thrusters	4	–
Thruster nominal thrust (each)	3.6	N
Total thrust	14.4	N
Specific impulse (I_{sp})	57	s
Propellant mass	5.0	kg
Total Δv capability	52.6	m/s
Burn duration (nominal)	70	s
System dry mass (tank, lines, valves)	2.3	kg
Total subsystem mass (wet)	7.3	kg

Overall, the entry propulsion system demonstrates that a purely cold-gas solution can provide adequate Δv control, precision targeting, and attitude stabilization for a low-mass Mars microprobe. The use of benign propellants, simple valving, and dual-use thrusters provides a fault-tolerant and mass-efficient path to reliable atmospheric entry for distributed planetary networks such as MAGPIE.

C. Probe Descent System

The descent system comprises a blunt aeroshell with an ablative heat shield and a two-stage parachute assembly consisting of a small supersonic drogue and a larger subsonic main canopy. This sequence provides attitude stabilization, aerodynamic drag modulation, and terminal velocity control over the full hypersonic–subsonic regime.

Aerodynamic Entry and Aeroshell Configuration. The aeroshell is a 1 m diameter, 70° half-angle sphere-cone derived from heritage Mars microprobe configurations [26]. Thermal protection is provided by a phenolic–carbon ablative (PICA-class) forebody, designed for peak heat fluxes of approximately 6.4 W/cm² and integrated load heating of 5.7 MJ/m², as determined from the entry simulation [28]. The ballistic coefficient of the entry configuration is $\beta_{EI} = 31.5 \text{ kg/m}^2$, optimized to achieve a peak dynamic pressure below 1.5 kPa while maintaining manageable deceleration levels (< 12 g). Following ablator burnout, the shield temperature remains below 820 K, ensuring full material margin.

The deceleration history during hypersonic entry can be estimated from the drag equation:

$$a_D = \frac{1}{2} C_D \frac{\rho V^2 A}{m}, \quad (106)$$

where C_D is the drag coefficient, ρ is the local atmospheric density, V is the velocity, A is the reference area, and m is the vehicle mass. For $\rho \approx 0.02 \text{ kg/m}^3$ and $C_D A/m = 1.2 \text{ m}^2/\text{kg}$, the resulting deceleration near peak dynamic pressure is on the order of 100 m/s² (10 g), consistent with simulation results [27]. Both of these methods of calculation were compared to previous Mars mission EDL profiles and the results were consistent [29].

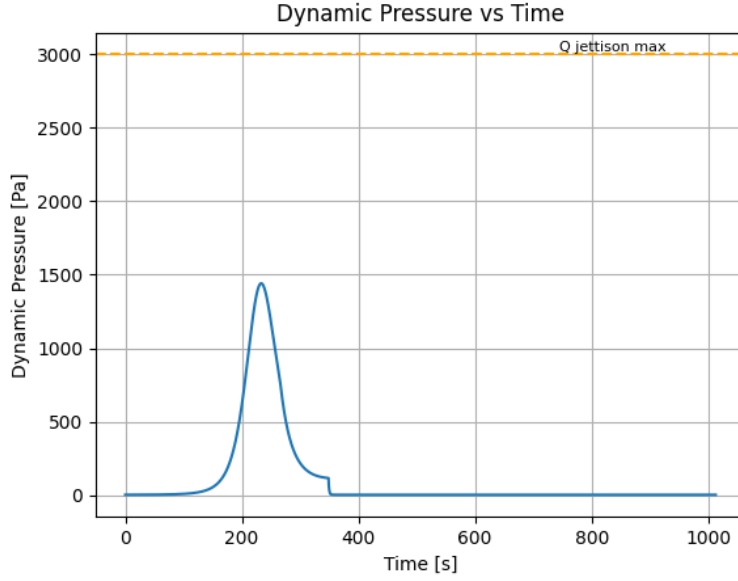


Fig. 25 Dynamic Pressure experienced by the Probe during EDL.

Drogue Parachute. The drogue parachute is a 0.30 m (1 ft) diameter, ribbon-type supersonic canopy deployed at approximately Mach 1.7 and altitudes of 25–30 km, corresponding to dynamic pressures of 700–900 Pa. Its function is primarily to stabilize the tumbling aeroshell during the transonic regime and to lower the ballistic coefficient for main-chute deployment. The drogue produces a drag force

$$D_{\text{drogue}} = \frac{1}{2} C_{D,\text{d}} \rho A_{\text{d}} V^2, \quad (107)$$

where $A_{\text{d}} = \pi(D_{\text{d}}/2)^2$ is the projected area. With $C_{D,\text{d}} \approx 1.2$ and $V \approx 450$ m/s, the initial drag contribution is roughly 500–700 N, corresponding to $\sim 1.5\text{--}2 g$ of deceleration.

Main Parachute. The main parachute is a disk-gap-band (DGB) canopy with a nominal diameter of 6.09 m and an effective drag coefficient $C_{D,\text{m}} \approx 2.1$. The canopy area is $A_{\text{m}} \approx 29.2 \text{ m}^2$ and the MAGPIE lander’s terminal mass is 33 kg. The average near-surface Martian atmospheric density expected is ($\rho_s \approx 0.020 \text{ kg/m}^3$) [30]. Balancing drag and weight gives the terminal velocity:

$$v_t = \sqrt{\frac{2mg_{\text{Mars}}}{C_{D,\text{m}}\rho_s A_{\text{m}}}}, \quad (108)$$

which yields a negative vertical velocity of $v_{\text{terminal}} \approx 14.11 \text{ m/s}$, corresponding to a full canopy diameter of roughly 3.05 m. This result aligns with preliminary EDL simulations, which predict a mean descent rate of 15 m/s during the chute phase with peak riser loads near 4.4 kN, well within the 25 kN riser design limit.

Deployment Logic and Cutaway Events. Both parachutes incorporate central spill holes for aerodynamic stability and load relief. Deployment is controlled via Mach number and dynamic pressure “corridor” checks in both the flight software and the EDL simulator:

$$M_{\text{deploy}} \in [0.3, 2.0], \quad q_{\text{deploy}} \in [50, 2000] \text{ Pa}, \quad (109)$$

ensuring each event occurs within a safe portion of the envelope. The drogue is automatically cut away upon main chute inflation, and the main canopy remains attached through landing unless a contingency cutaway command is triggered for stability reasons.

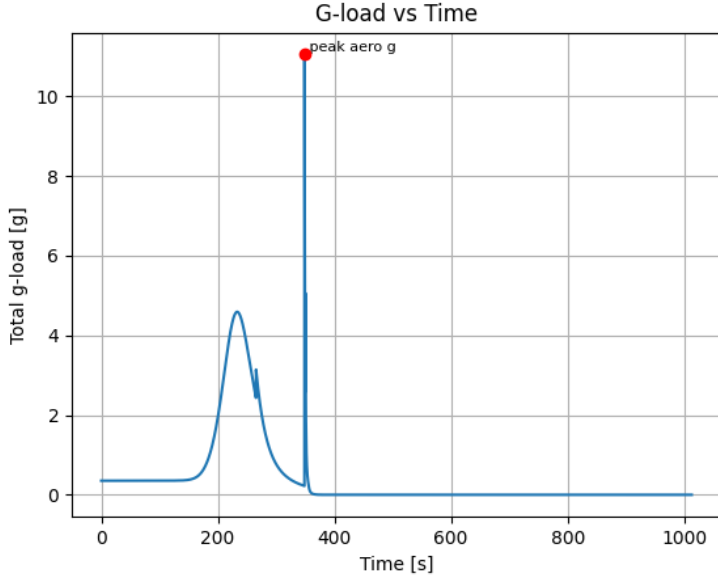


Fig. 26 G-Loading Experienced by the Probe during EDL. Note Max G-Loading occurs during main chute inflation.

Design Philosophy. In contrast to complex EDL systems such as the Mars Skycrane [29] or retropropulsive landers, MAGPIE intentionally accepts a higher impact velocity in exchange for simplicity, reliability, and reduced system mass. The entire descent phase involves only two pyrotechnic events (drogue release and main deployment), no powered descent, and no attitude thrusters. The system therefore emphasizes *passive robustness*: stability through geometry, energy absorption through structure, and tolerance of off-nominal conditions without active control. This approach minimizes potential single-point failures and keeps the total descent subsystem mass below 2.5 kg while achieving survivable touchdown loads verified through numerical EDL simulations.

D. Probe Landing System

Even with the main parachute, the MAGPIE probe impacts the surface at approximately 12–13 m/s, corresponding to a kinetic energy on the order of 2.3 kJ for a 33 kg terminal mass. To protect the avionics, batteries, and sensors within the primary bus, a dedicated aluminum honeycomb crush structure is mounted beneath the lander. This structure plastically deforms under load, converting translational kinetic energy into quasi-static crushing work over a prescribed stroke length.

The landing event is governed by an energy balance between the probe’s kinetic energy at touchdown and the mechanical work done by the honeycomb as it crushes:

$$E_{\text{impact}} = \frac{1}{2}mv_t^2, \quad E_{\text{abs}} = \sigma_p As, \quad (110)$$

where m is the lander mass, v_t is the vertical velocity at contact, σ_p is the plateau (crush) stress of the core material [31], A is the effective footprint area, and s is the available crush stroke. For a safe, fully absorbed landing,

$$E_{\text{abs}} \geq E_{\text{impact}}. \quad (111)$$

The required plateau stress to just arrest the vehicle within the available stroke is therefore:

$$\sigma_{\text{req}} = \frac{mv_t^2}{2As}. \quad (112)$$

For the nominal MAGPIE configuration ($m = 33.1$ kg, $v_t = 11.8$ m/s, $A = 0.503$ m 2 , $s = 0.05$ m), this yields $\sigma_{\text{req}} \approx 0.09$ MPa, which closely matches the simulated value of 0.082–0.091 MPa [31]. The corresponding deceleration

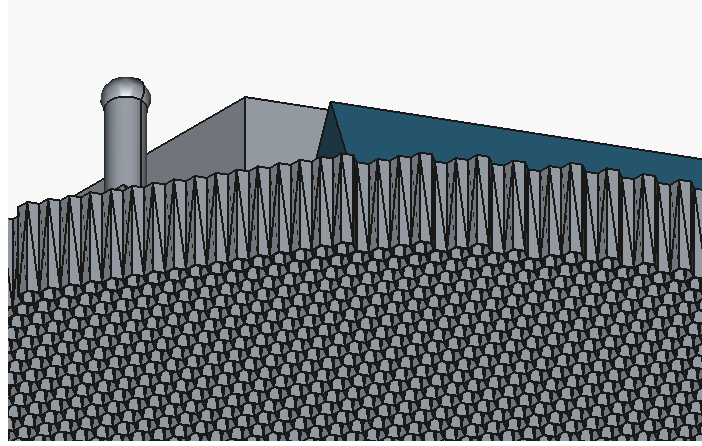


Fig. 27 View of the honeycomb crush core of the MAGPIE probes.

can be estimated as:

$$a_{\text{avg}} = \frac{\sigma_p A}{m g_{\text{Mars}}}, \quad (113)$$

giving an average of ~ 140 g at Mars gravity, consistent with the entry–descent–landing (EDL) simulation.

The honeycomb mechanical behavior is characterized by its relative density ρ^*/ρ_s and a material-dependent efficiency factor C_σ , which together define the plateau stress:

$$\sigma_p = C_\sigma \sigma_y \left(\frac{\rho^*}{\rho_s} \right)^2, \quad (114)$$

where σ_y and ρ_s are the yield strength and density of the solid material, respectively. Aluminum 5052 or 3003 cores with $\sigma_y \approx 120$ MPa and $\rho_s = 2700$ kg/m³ provide an efficient combination of strength and manufacturability for low-mass applications [31]. The effective C_σ used in MAGPIE’s baseline configuration is ~ 0.014 , corresponding to a relative density of 0.048, yielding a plateau stress near 0.08 MPa [32].

To remain within the design deceleration limit of 300 g, the honeycomb parameters must satisfy:

$$\sigma_p \leq \frac{m g_{\text{lim}}}{A}, \quad (115)$$

where g_{lim} is the acceptable peak acceleration of the payload. For $g_{\text{lim}} = 300$ g, this corresponds to $\sigma_p \lesssim 0.19$ MPa, leaving ample safety margin.

The resulting system is therefore tuned such that the full 50 mm crush stroke is utilized without structural bottoming, placing the landing in the *stroke-limited* regime. In this mode, peak loads can be reduced most effectively by increasing the crush distance or the footprint area rather than further lowering the core stiffness. Larger area or taller honeycomb blocks would proportionally reduce the transmitted deceleration [31]:

$$a_{\text{peak}} \propto \frac{1}{sA}. \quad (116)$$

This energy-absorbing landing architecture allows MAGPIE to meet its payload survivability requirements using lightweight, commercially available aluminum honeycomb cores, similar in principle to those qualified for prior Mars microprobe and airbag systems [33]. The overall design achieves a simulated maximum deceleration of 141 g and an impact energy absorption efficiency exceeding 90%, with substantial margin to the structural and electronics limits.

E. EDL Summary

The MAGPIE probe EDL architecture is intentionally simple and margin-rich. A brief cold-gas deorbit ($\Delta v = 52.6$ m/s) from a 250 km circular orbit targets a 35 km periapsis and an entry interface near 125 km at ~ 3.5 km/s. A 1.0 m, 70° sphere–cone aeroshell with low ballistic coefficient ($\beta \approx 27.4$ kg/m²) provides passive hypersonic

stability and keeps peak dynamic pressure below ~ 1.5 kPa and peak deceleration to $\sim 10\text{--}12 g$ (nominal atmosphere). Sutton–Graves estimates and CFD-informed coefficients bound the stagnation convective environment to $\sim 6\text{--}7 \text{ W/cm}^2$ peak and $\sim 5\text{--}6 \text{ MJ/m}^2$ total heat load for PICA-class TPS sizing.

Through transonic, a small ribbon drogue deployed near $M \approx 1.7$ at 25–30 km trims residual rates and hands off to a DGB main canopy sized to achieve $v_t \approx 12\text{--}15 \text{ m/s}$ in near-surface densities ($\rho_s \approx 0.020 \text{ kg/m}^3$). The probe impacts on a tuned aluminum-honeycomb crush core (stroke $\sim 50 \text{ mm}$, footprint $\sim 0.5 \text{ m}^2$) that absorbs $>90\%$ of the $\sim 2\text{--}3 \text{ kJ}$ impact energy and limits transmitted loads to $\sim 140 \text{ g}$ average with ample margin to a 300 g design cap. No powered terminal descent is required.

Nominal timeline (representative of landing site):

- **Deorbit:** $\Delta v = 52.6 \text{ m/s}$ cold-gas burn ($\sim 70 \text{ s}$), attitude trimmed via reaction wheels / thrusters; EFPA set.
- **Entry Interface:** $h \approx 125 \text{ km}$, $V \approx 3.5 \text{ km/s}$; hypersonic lift/drag from sphere-cone ($L/D \approx 0.16$).
- **Peak heating / q :** $\sim 35\text{--}45 \text{ km}$; TPS sized to $\sim 6\text{--}7 \text{ W/cm}^2$ peak, $\sim 5\text{--}6 \text{ MJ/m}^2$ load.
- **Aeroshell jettison:** $\sim 25\text{--}30 \text{ km}$; **Drogue deploy:** $M \approx 1.7$, $q \in [700, 900] \text{ Pa}$.
- **Main deploy:** subsonic corridor checks ($M \in [0.3, 0.8]$, $q \in [50, 2000] \text{ Pa}$); descent at 12–15 m/s.
- **Touchdown:** honeycomb crush, full-stroke, no bottoming; payload loads $\sim 140 \text{ g}$ avg, $<300 \text{ g}$ peak.

Margins and sensitivities. Monte-Carlo dispersions in mass ($\pm 10\%$), density ($\pm 20\%$), and winds (TRL heritage profiles) indicate: (i) peak g remains $<15 \text{ g}$ for hypersonic deceleration with $\beta \lesssim 32 \text{ kg/m}^2$; (ii) canopy loads remain within riser limits with the Mach/dynamic-pressure corridor logic; (iii) terminal v_t varies $\sim \pm 2 \text{ m/s}$ across ρ_s and C_D bounds, still within crush-core absorption capacity. Overall EDL probability-of-success is driven more by atmospheric density outliers and deploy timing than by TPS or crush-core margins; both subsystems retain $> 30\%$ performance margin at the 3σ design point.

Design philosophy. The system trades pinpoint landing for *robust simplicity*: no throttled terminal propulsion, two pyrotechnic events, passive aero stability, and structural energy absorption. CFD-informed aerodynamics close the heating and deceleration budgets; parachute corridors and cutaway logic bound inflation risk; and the crush structure linearizes touchdown variability. In aggregate, the reference configuration safely delivers the probe under allowable thermal, structural, and deceleration limits for the modeled atmospheres while preserving mass and operational simplicity for a six-probe network.

IX. Probe Environmental, Power, and Thermal Analysis

A. Simulation Overview

A 700-hour simulation (30 s time step) was run with cork-only insulation ($R_{\text{skin} \rightarrow \text{int}} = 5.26 \text{ K/W}$, $R_{\text{int} \leftrightarrow \text{batt}} = 1.67 \text{ K/W}$) and optical depth $\tau = 0.4$. Internal and battery multilayer insulation (MLI) layers were disabled to assess worst-case conduction to the environment and to highlight the performance achievable with a minimal insulation stack [34].

B. Results Summary: Hellas Planitia Baseline (MAGPIE-2)

A 700-hour simulation (30 s timestep) was executed for the MAGPIE-2 probe, assumed to land within central Hellas Planitia ($\sim 45^\circ\text{S}$, $\sim 70^\circ\text{E}$) during mid-autumn under moderate dust loading ($\tau = 0.4$). This location provides a representative average of Martian solar levels and thermal environment, making it the baseline case for assessing long-term power–thermal performance.

The configuration employed cork-only insulation ($R_{\text{skin} \rightarrow \text{int}} = 5.26 \text{ K/W}$, $R_{\text{int} \leftrightarrow \text{batt}} = 1.67 \text{ K/W}$), with internal and battery multilayer insulation (MLI) layers disabled to evaluate worst-case conduction and radiative exchange with the environment. In the actual design, the probe, battery, and electronics compartment will all be lined with a 3 mm-thick MLI layer. This will add significant thermal insulation to the probe and help to maintain more constant conditions.

The system remains power-positive throughout the simulation, maintaining SOC ≥ 0.20 and keeping all thermal nodes above their survival thresholds. No brownouts or heater anomalies were observed, and peak solar power exceeded 310 W, confirming a comfortable margin for housekeeping and communication loads even under moderate optical depth.

Table 15 MAGPIE-2 (Hellas Planitia) Power–Thermal Performance Summary (700 hr Simulation)

Parameter	Value	Units
Final SOC	0.464	–
Min SOC	0.195	–
Heater duty	72.6	%
Heater energy	2539.7	Wh
Harvested energy	19988.1	Wh
Load consumption	1681.9	Wh
Peak panel output	163.98	W
Min temperatures (skin/int/batt)	-76.1/-33.5/-25.9	°C

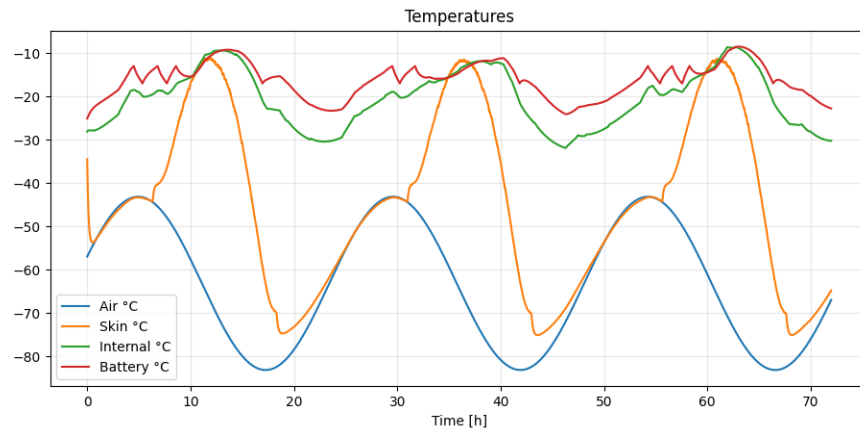


Fig. 28 Simulated probe temperature for MAGPIE-2 over the course of 72 hours. The sawtooth waveform reflects the heater cycling on and off to prevent excessive power draw.

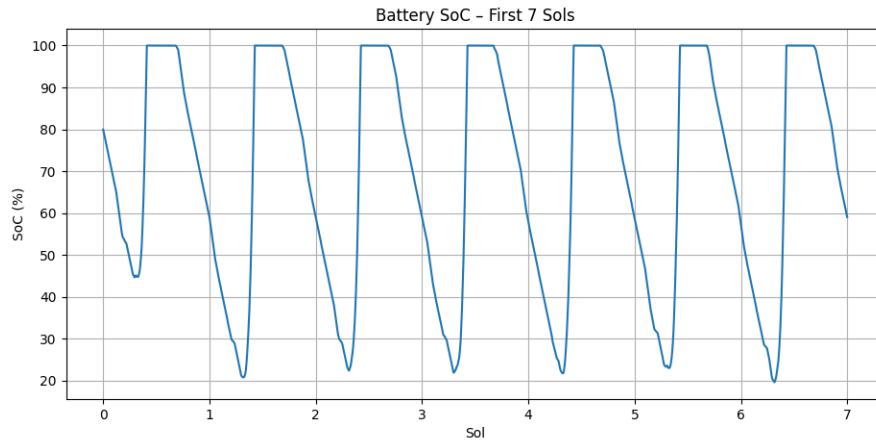


Fig. 29 Battery state of charge (SOC) over seven sols of simulated operation for the Hellas Planitia baseline case.

C. Comparative Site Outcomes

While Hellas Planitia represents the nominal, energetically balanced case, additional simulations were conducted for the remaining MAGPIE probes to establish operational margins across a range of latitudes and environments. These

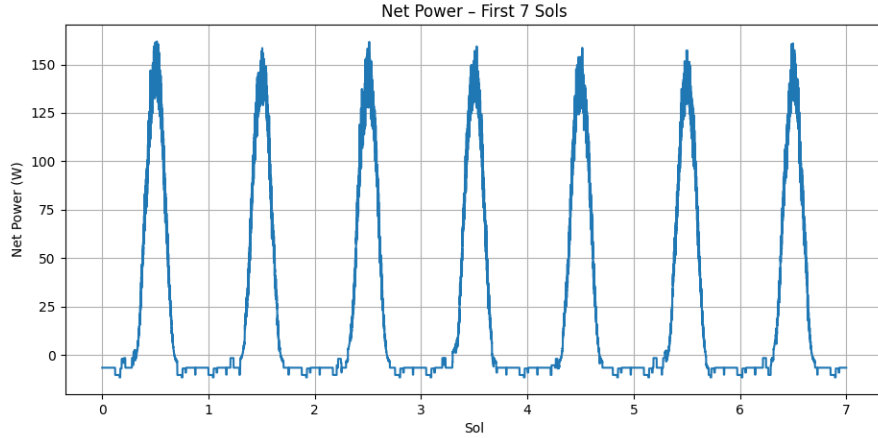


Fig. 30 Net electrical power over seven sols of simulated operation for the Hellas Planitia baseline case.

include the polar, equatorial, and northern mid-latitude sites summarized below.

- **MAGPIE-1 (Olympus Mons, 18.65°N):** Due to its ideal latitude, MAGPIE-1 is able to generate large amounts of power, 84.7 kWh over the duration of the mission (28 sols). As a result, it is a prime landing site for a MAGPIE Probe.
- **MAGPIE-3 (Planum Boreum, 87.98°N):** Experiences continuous heater demand above 80% due to the limited solar elevation and low surrounding temperatures. Total energy collected over 28 sols is 2570 Wh, leading to full depletion and shutdown within ~72 h.
- **MAGPIE-4 (Planum Australis, 83.9°S):** Experiences continuous heater demand above 80% due to limited solar elevation and low ambient temperatures. Total energy collected over 28 sols is 857 Wh, leading to full depletion and shutdown within ~32 h. This is the fastest loss of any probe, but it will be launched last in order to verify that the other probes are actively collecting data at the same time.
- **MAGPIE-56 (Example Site: Argyre Planitia, 45°N):** Produces 38.1 kWh and has stable internal temperatures throughout the run. Slightly improved solar gain relative to Hellas Planitia offsets colder ambient conditions.

Table 16 Summary of site-dependent energy and survival outcomes (700 h simulations, $\tau = 0.4$)

Landing Site	Lat (deg)	P_{tot} (Wh)	P_{peak} (W)	ToD (h)	Final/Min SOC	$Heater_{\text{duty}}$ (%)	Batt Temp _{min}
MAGPIE-1	18.65° N	84675.4	540.85	inf	100/35.3	47.5	-24.6
MAGPIE-2	42.4° S	45057.2	317.75	inf	100/29.5	57.9	-25.9
MAGPIE-3	87.98° N	2569.6	5.61	72	8/0	83.8	-26.2
MAGPIE-4	83.9° S	856.8	4.95	32	3/0	90.6	-27.9

Across all locations, the MAGPIE architecture demonstrates robust performance for equatorial and mid-latitude deployments, maintaining continuous operation even under moderate dust loading. Polar sites, however, show rapid SOC depletion due to low solar incidence and high heater demand, emphasizing the need for adaptive thermal management and site-specific landing season selection.

Future analyses will extend this dataset to additional latitudes, optical depths, and seasonal conditions, enabling a statistical survivability model for the full six-probe network using climatological data from MCS and TES.

X. Expected Science Outcomes

MAGPIE will yield the first time-synchronous, multi-latitude dataset of Martian near-surface meteorology and electrification. These data will:

- Quantify spatial gradients in temperature, pressure, and electric field strength;
- Characterize boundary-layer turbulence and dust mobilization thresholds;

- Constrain models of charge separation and dust electrification in weakly conducting atmospheres;
- Improve EDL simulations using real surface density and wind profiles at entry interface conditions.

The integration of acoustic, optical, and electrical sensing enables cross-domain analyses beyond the scope of single-site missions such as *Viking*, *InSight*, and *Perseverance*. MAGPIE thus bridges the gap between point measurements and global circulation models, informing both fundamental science and engineering design.

A. Radio Occultation

Radio occultation (RO) is employed to retrieve vertical profiles of atmospheric refractivity, density, and temperature by analyzing the bending of a coherent radio signal as it passes tangentially through the Martian atmosphere. As the orbiter–probe geometry evolves during an occultation event, the transmitted carrier experiences refraction proportional to the local refractive index gradient. This bending effect, measurable from Doppler shift variations, provides an indirect but highly precise probe of atmospheric structure.

The total bending angle $\alpha(a)$ at impact parameter a is defined as the cumulative deflection of the signal as it traverses a spherically stratified medium with refractive index $n(r)$:

$$\alpha(a) = -2a \int_{r_a}^{\infty} \frac{d \ln n(r)}{dr} \frac{dr}{\sqrt{(nr)^2 - a^2}}, \quad (117)$$

where r_a is the radius of closest approach. Inverting this relationship via the Abel transform yields the refractive index profile [35]:

$$n(r) = \exp \left[\frac{1}{\pi} \int_a^{\infty} \frac{\alpha(a') da'}{\sqrt{a'^2 - a^2}} \right]. \quad (118)$$

The refractivity N is then related to local atmospheric pressure P and temperature T through:

$$N = (n - 1) \times 10^6 = k_1 \frac{P}{T} + k_2 \frac{P_w}{T^2}, \quad (119)$$

where k_1 and k_2 are empirically derived refractivity constants and P_w is the partial pressure of water vapor [35]. For the predominantly CO₂ Martian atmosphere, the second term is negligible, simplifying retrievals.

In the MAGPIE configuration, each probe–orbiter pair conducts one-way radio occultation experiments during entry, descent, or overpass geometries using coherent UHF and S-band carriers. The derived bending angle profiles are processed through Abel inversion to reconstruct vertical temperature and density profiles with sub-kilometer resolution in the lower atmosphere. This technique provides crucial context for in-situ meteorological and electrical measurements, enabling cross-validation of thermal gradients and boundary-layer dynamics.

XI. Relevance and Broader Impacts

MAGPIE directly addresses long-standing gaps in Mars atmospheric science by enabling simultaneous, latitudinally distributed measurements of the near-surface environment. Prior landed missions—including *Viking*, *Phoenix*, *Curiosity*, and *InSight*—have produced high-quality but geographically isolated datasets. Their single-point measurements limit the ability to constrain diurnal circulation, turbulent fluxes, dust lifting thresholds, and atmospheric electricity across different terrain, seasons, and latitudes. MAGPIE’s coordinated descent and multi-site landed observations uniquely overcome these limitations by providing globally contextualized, synchronized datasets of boundary-layer structure and surface–atmosphere coupling.

The mission’s distributed probe network also enables direct validation of mesoscale and general circulation models (GCMs), facilitating improved prediction of temperature gradients, nighttime inversions, dust lofting, and transient meteorological events. These measurements will refine EDL aerodynamics, heating estimates, and surface-wind climatology—providing stronger environmental margins for future robotic and crewed landed systems.

Beyond its scientific objectives, MAGPIE’s architecture demonstrates a scalable, low-cost approach to planetary exploration. The use of repeatable microprobe units; standardized avionics and sensors; commercial reaction wheels, radios, and power components; and composite/3D-printed structures enables rapid manufacturing and mission customization at modest cost. The single-orbiter relay concept reduces operational complexity and allows deployment of multiple probes without requiring multiple launches or orbiters.

This architecture is extensible to other destinations. Variants of the MAGPIE platform could support Earth–Moon environmental monitoring, asteroid regolith surveying, atmospheric profiling at Venus or Titan, or distributed

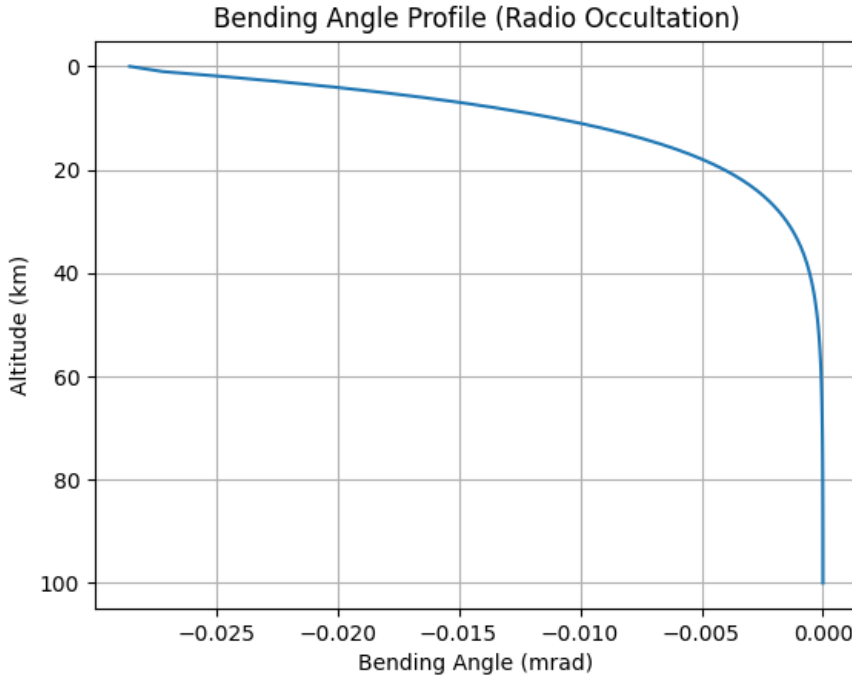


Fig. 31 Computed bending angle profile from the MAGPIE radio occultation simulator, showing the progressive signal curvature as a function of altitude.

magnetospheric measurements. The design's modularity is compatible with university-class payloads, international partnerships, and commercial technology demonstrations, aligning with NASA's goals for sustainability and reusability in exploration systems.

Aligned with the *Planetary Science and Astrobiology Decadal Survey 2023–2032*, MAGPIE advances the priority science themes of “Climate and Surface–Atmosphere Interactions,” “State and Evolution of the Martian Environment,” and “Preparation for Human Exploration.” By quantifying diurnal and seasonal variability in boundary-layer dynamics, dust transport, and atmospheric electrification across a full pole-to-pole transect, MAGPIE provides critical inputs for surface hazard forecasting, ISRU system design, and habitat thermal modeling. Its replicable, networked architecture directly supports the Decadal recommendation to deploy distributed surface assets capable of producing simultaneous, globally relevant datasets.

XII. Conclusion

This study explores a mission framework for deploying a distributed network of low-mass atmospheric probes to Mars using a single medium-class launch vehicle. Within this context, trajectory and propulsion analyses indicate that a 7.5 t orbiter–probe stack can meet the $C_3 = 9.879 \text{ km}^2/\text{s}^2$ trans-Mars injection requirement and close a $\Delta v_{\text{MOI}} = 1.49 \text{ km s}^{-1}$ orbit-insertion sequence with reasonable margins under typical modeling assumptions.

Entry–descent–landing simulations suggest that compact, 23 kg probes enclosed in 1 m, 70° sphere–cone aeroshells can survive the expected range of atmospheric and surface conditions. Modeled deceleration loads, terminal descent speeds, crush-core response, and heating levels remain within the bounds of well-characterized materials and structures. While uncertainties remain in atmospheric dispersion and parachute performance, the results provide an initial indication that such probes can deliver usable payloads to diverse latitudes.

Thermal-power modeling conducted over a 700 hour window offers a preliminary view of landed survivability. Mid-latitude sites show potential for multi-sol operation with moderate dust loading, whereas polar deployments are more constrained, typically supporting operational windows on the order of tens of hours. These outcomes underscore the importance of latitude, season, and dust conditions in shaping small-probe mission design.

The orbiter’s attitude-control concept—based on commercially available reaction wheels, redundant star trackers, and UHF/LoRa relay antennas—demonstrates that a modest spacecraft can provide both probe relay and X-band DSN downlink while maintaining required pointing accuracy. The expected link margins at 1.5 AU are consistent with current small-to-medium planetary mission capabilities.

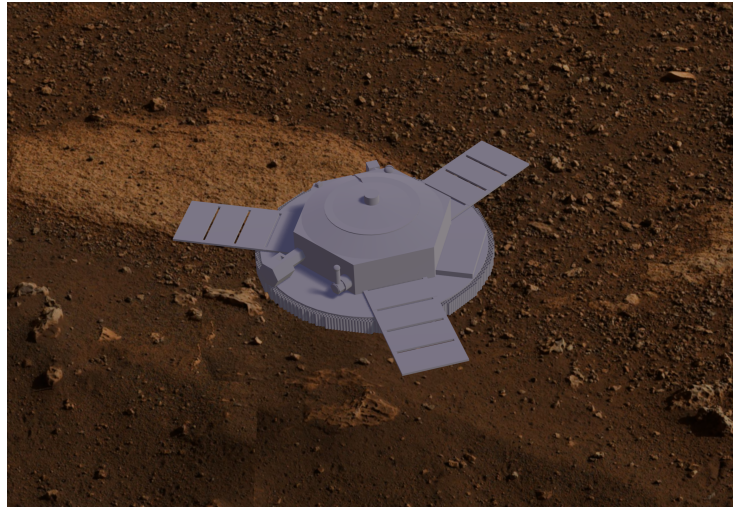


Fig. 32 A deployed and landed MAGPIE probe on the surface of Mars.

Overall, the MAGPIE analysis should be viewed as an initial framework rather than a finalized design. It highlights how distributed, low-cost probes, combined with a simple relay orbiter, may enable simultaneous, multi-latitude measurements of Martian boundary-layer processes and atmospheric electricity. The results point toward a scalable, repeatable approach that could support future investigations of Mars’ near-surface environment, technology demonstrations, or broader planetary network concepts.

A. Future Work

Future development of MAGPIE will focus on the following: higher-fidelity modeling, hardware prototyping, and systems integration.

- **Enhanced modeling and validation.** Expansion of the current simulation suite to include 6-DOF entry dynamics, aerothermal ablation modeling using Sutton–Graves correlations, and detailed communication link analysis under realistic orbital geometries. Power–thermal simulations will be extended to include dust deposition, panel degradation, and probabilistic illumination modeling based on Mars Climate Database (MCD) inputs.
- **Hardware and subsystem prototyping.** Construction of a full-scale engineering model of the microprobe structure, crush-core, and avionics stack for vibration and thermal-vacuum testing. A benchtop power and communications testbed will validate inter-probe and orbiter relay protocols, with a focus on link margins at low

elevation angles ($< 10^\circ$).

- **Mission design refinement.** Phase A trade studies will explore alternative orbiter configurations (e.g., solar-electric relay variant), optimization of probe release geometry, and potential expansion to 8–10 probes for enhanced temporal coverage. Launch vehicle trades will also be updated with performance curves for Falcon Heavy and Vulcan Centaur to validate secondary payload compatibility.

Collectively, these next steps will advance MAGPIE from concept-level feasibility to prototype validation, bridging the gap between analytical modeling and an executable distributed Mars mission. The mission’s framework—scalable, redundant, and leveraging commercial off-the-shelf (COTS) technologies—positions it as both a scientific pathfinder and a practical template for future networked planetary surface architectures.

Acknowledgments

The author would like to thank Paige Rust and Nathaniel Polus, who provided feedback on the MAGPIE concept and the associated simulations in support of this paper. The author would also like to thank everyone who has worked on any open-source library, software, or project. This entire project was completed with open-source software and thus, could not be done without it.

References

- [1] Curtis, H. D., *Orbital mechanics for engineering students*, Butterworth-Heinemann, 2019.
- [2] Chicarro, A., Martin, P., and Trautner, R., “The Mars Express mission: an overview,” In: *Mars Express: the scientific payload*. Ed. by Andrew Wilson, scientific coordination: Agustin Chicarro. ESA SP-1240, Noordwijk, Netherlands: ESA Publications Division, ISBN 92-9092-556-6, p. 3–13, Vol. 1240, 2004, pp. 3–13.
- [3] SpaceX, “Falcon 9,” , 2024. URL <https://www.spacex.com/vehicles/falcon-9/>, accessed 2024–2025.
- [4] Larson, W. J., and Wertz, J. R., “Space Mission Analysis and Design,” 1999.
- [5] Blue Origin, “New Glenn Launch Vehicle Specifications,” , 2025. URL <https://www.blueorigin.com/new-glenn>.
- [6] NASA Launch Services Program, “New Glenn Capabilities and Pricing (Industry Summary),” , 2024. URL <https://www.nasa.gov/directorates/heo/lsp/>, compiled from NASA LSP commercial capability data; accessed 2024–2025.
- [7] European Space Agency (ESA), “Ariane 6 Launcher,” , 2024. URL https://www.esa.int/Enabling_Support/Space_Transportation/Ariane_6, accessed 2024–2025.
- [8] ArianeGroup, “Ariane 6 Pricing and Performance Overview,” , 2024. URL <https://www.ariane.group/launch-services/ariane-6/>, accessed 2024–2025.
- [9] China Aerospace Science and Technology Corporation (CASC), “Long March 5 Launch Vehicle,” , 2024. URL <https://english.spacechina.com/n17212/n17281/n17298/index.html>, accessed 2024–2025.
- [10] Zhang, Y., et al., “The Long March 5 Launch Vehicle: Configuration and Mission Capability,” *Journal of Astronautics*, Vol. 43, 2022, pp. 330–345. Includes cost/performance data used in trade analyses.
- [11] United Launch Alliance, “Vulcan Centaur Rocket,” , 2024. URL <https://www.ulalaunch.com/rockets/vulcan>, accessed 2024–2025.
- [12] United Launch Alliance, “ULA Vulcan Pricing and Capability,” , 2024. URL <https://www.ulalaunch.com>, accessed 2024–2025.
- [13] Roscosmos State Corporation, “Proton-M Launch Vehicle,” , 2023. URL <https://www.roscosmos.ru/>, accessed 2024–2025.
- [14] International Launch Services (ILS), “Proton-M/Briz-M User’s Guide (International Launch Services),” , 2021. URL <https://www.ilslaunch.com>, contains cost+mass data; accessed 2024.
- [15] RTD Embedded Technologies, Inc., *PC/104-Plus AMD Geode LX CPU Module: CME137686LX Series*, RTD Embedded Technologies, Inc., State College, PA, 2024. URL <https://www.rtd.com/PC104/CM/686/137686/CME137686LX.htm>, technical specifications for the CME137686LX PC/104-Plus SBC with AMD Geode LX800 processor, 256–512 MB DDR SDRAM, and onboard flash storage.

- [16] Kirby, K., Gupta, K., Smith, E., and Brewer, K., “Mitigation of High Altitude and Low Earth Orbit Radiation Effects on Microelectronics via Shielding or Error Detection and Correction Systems,” Tech. rep., NASA Glenn Research Center and Prairie View A&M University, Cleveland, OH, 2004. URL <https://ntrs.nasa.gov/>, final report under NASA Cooperative Agreement NAG4-210.
- [17] Kaplan, M. H., *Modern spacecraft dynamics and control*, Courier Dover Publications, 2020.
- [18] Huang, J., and Imbriale, W., “Spacecraft antenna research and development activities aimed at future missions,” *Spaceborne Antennas for Planetary Exploration*, 2006, pp. 485–536.
- [19] Northrop Grumman Innovation Systems, *Northrop Grumman Propulsion Products Catalog*, Northrop Grumman, Promontory, UT, 2016. URL <https://www.northropgrumman.com/space/propulsion-systems/>, comprehensive product catalog of Orion, STAR, CASTOR, GEM, and SLS-class solid rocket motors. Approved for Public Release OSR No. 16-S-1432.
- [20] Khaleelullah, A., Basha, S. J., and Rangavittal, H., “Design and analysis of propellant tanks support structure for an advanced spacecraft,” *Int. J. Appl. Res. Mech. Eng.*, Vol. 2, 2011, pp. 75–81.
- [21] “Mars Microprobe (Deep Space 2) Flight Results and Lessons Learned,” Tech. Rep. 19990036014, NASA / Jet Propulsion Laboratory, 1999. Probe architecture, EDL performance, and post-flight assessment.
- [22] Sidi, M. J., *Spacecraft dynamics and control: a practical engineering approach*, Vol. 7, Cambridge university press, 1997.
- [23] Wertz, J. R., Everett, D. F., and Puschell, J. J., “Space mission engineering: the new SMAD,” (*No Title*), 2011.
- [24] Greenshields, C. J., *OpenFOAM v13 User Guide*, The OpenFOAM Foundation, London, UK, 2025. URL <https://doc.cfd.direct/openfoam/user-guide-v13>.
- [25] OpenCFD Ltd., “OpenFOAM User Guide, Version v2506,” , June 2025. URL <https://www.openfoam.com/documentation>.
- [26] McGrew, L. C., Killeen, B. J., and Mendeck, G. F., “Entry Guidance Design and Post-Flight Performance of the Mars 2020 Mission,” *AIAA/AAS SciTech*, 2025. Bank-angle range control and Jezero landing performance assessment.
- [27] Bhaskaran, R., and Stern, E. C., “Scale-Resolving Simulations of Viking ’75 Reentry Capsule Wake Flow,” *AIAA SciTech Forum*, NASA Ames Research Center, Moffett Field, CA, 2023. Comparison of US3D and PyFR solvers for Viking ’75 reentry capsule wake flow across subsonic and transonic Mach regimes; DOI to be added from AIAA Digital Library.
- [28] “Entry Data Analysis for the Viking Preflight Design Studies,” Tech. Rep. 19720003329, NASA, Washington, DC, 1972. Aerothermodynamics and entry dispersion analyses supporting Viking.
- [29] Steltzner, A. F., Eisen, H., Manning, R., Brazzel, J.-M., et al., “Mars Science Laboratory Entry, Descent, and Landing System Overview,” Tech. Rep. 20090024230, NASA / Jet Propulsion Laboratory, 2009. System architecture, performance margins, and flight design summary.
- [30] Pereira, J., Cruz, J., and colleagues, “Mars Exploration Rover Parachute Decelerator System: Design and Qualification,” *AIAA Conference*, 2004. MER DGB design, scaling, testing, and qualification results.
- [31] Wei, W., Zhang, S., Zhao, X., Quan, X., Zhou, J., Yu, N., Wang, H., Li, M., and Hou, X., “Research on aluminum honeycomb buffer device for soft landing on the lunar surface,” *International Journal of Aerospace Engineering*, Vol. 2021, No. 1, 2021, p. 7686460.
- [32] Rogers, W. F., “Apollo Experience Report - Lunar Module Landing Gear Subsystem,” Tech. Rep. NASA TN D-6850, Manned Spacecraft Center, Houston, TX, 1972. URL <https://ntrs.nasa.gov/>, report on the Apollo Lunar Module Landing gear and how the subsystem is built, designed, and how it preformed.
- [33] Dutta, S., Karlgaard, C. D., Tynis, J. A., O’Farrell, C., Sonneveldt, B. S., Queen, E. M., Bowes, A. L., Leylek, E. A., and Ivanov, M. C., “Advanced Supersonic Parachute Inflation Research Experiments: Pre-flight Trajectory Modeling and Post-flight Reconstruction,” *AIAA SciTech / Flight Mechanics*, 2019. ASPIRE SR01/SR02/SR03 Mars-relevant DGB tests; targeting and reconstruction.
- [34] Stella, P. M., and Herman, J. A., “The Mars surface environment and solar array performance,” *2010 35th IEEE Photovoltaic Specialists Conference*, IEEE, 2010, pp. 002631–002635.
- [35] Schreiner, W. S., Weiss, J., Anthes, R. A., Braun, J., Chu, V., Fong, J., Hunt, D., Kuo, Y.-H., Meehan, T., Serafino, W., et al., “COSMIC-2 radio occultation constellation: First results,” *Geophysical Research Letters*, Vol. 47, No. 4, 2020, p. e2019GL086841.